DFT, EPR and SPR insight to the relation between photocatalytic activity and nonlinearity and anisotropy ferromagnetism of Au/Co3O4/Bi2MoO6 composites

DFT, EPR and SPR insight to the relation between photocatalytic activity and nonlinearity and anisotropy ferromagnetism of $Au/Co_3O_4/Bi_2MoO_6$ composites

Qiuling Chen*[1], Baoji Miao[1], Yinlei Hao[2], Hui Wang [1], Qiuping Chen[3]

[1]Materials science and technology department, Henan University of Technology, Lianhua road 100, Zhengzhou, 450001, China

[2]Shenzhen Institute of Zhejiang University, Shenzhen, China

[3] Applied Science Technology, Politecnico di Torino, corso duca degli abruzzi, 24, Torino, italy

*qiulingchen1972@gmail.com

Abstract:

The combination of Surface Plasmon Resonance (SPR) effect with hetero-p-n structure has shown promising benefits to photocatalytic activity of catalysts. In this study, Au nanoparticles doped p-n hetero-structured Co_3O_4/Bi_2MoO_6 composites were synthesized and subjected to photocatalytic and photocurrent tests using visible light irradiation. The synthesized $Au/Co_3O_4/Bi_2MoO_6$ efficiently removed 97.2 % of Methyl orange within 60 min, showing very good photocatalytic stability through leaching test. Colorless pollutant phenol degradation test verified the excellent photocatalytic activity of $Au/Co_3O_4/Bi_2MoO_6$. Possible influential factors such as electron transition, charge transfer, energy band gap, DOS, polarizability, SPR effect, oxygen vacancies and anisotropy permittivity were investigated through DFT, XPS, EPR, Z-scan, UV-visible spectra, ellipsometer spectroscopy and Mott-Schottky analysis. A reasonable degradation mechanism and possible pathway for Methyl orange were proposed based on the experimental results and DFT calculations. The doped Co_3O_4 provided active 3*d* electrons transition and charge transfer which increased carriers' concentration and reduced the energy band gap, while the Au SPR enhanced internal polarization and strengthened the built-in electric field, yielding strong driving force for photo-generated electrons-holes pairs separation and consumption. In addition, magnetic Co_3O_4 endowed sample with room-temperature ferromagnetism which was obviously strengthened by Au NPs. The magnetism of sample was beneficial for separation and recovery in photocatalytic practical applications.

Keywords: Photo-catalysis, Nonlinearity, Ferromagnetism, $Au/Co_3O_4/Bi_2MoO_6$

Introduction

Novel functionalized perovskite photocatalytic materials with high photocatalytic activity are currently desired [1]. Aurivillius-phase perovskite Bi_2MoO_6 (BMO) has unique MoO_4^{2-} - $[Bi_2O_2]^{2+}$ layered structure and can exhibit O 2p and Bi 6s hybrid orbitals. These features have endowed BMO high oxidative activity, large charge-carrier mobility and importantly relatively narrow and promising band gap energy (2.4-2.9 eV) for photocatalytic application [1 - 4].

Due to the layered structure of BMO, various p-n heterojunctions [3-8] have been constructed to improve photocatalytic performance. Such as $Bi_2MoO_6/CuBi_2O_4$ heterojunctions [3],

$CdS/Bi_2MoO_6/BiOBr$ [6], $Bi_2Sn_2O_7/Bi_2MoO_6$ [7] and Ta_3N_5/Bi_2MoO_6 [8]. Among p-type semiconductors, thanks to its high stability and strong light adsorption, Co_3O_4 doped Co_3O_4/CdS [9], Bi_2MoO_6 [10] have exhibited improved photo-electrochemical and photocatalytic behavior because the Co^{2+} and Co^{3+} ions in Co_3O_4 offered good to charge carriers and electron transition. In addition, the Co_3O_4 could help to form oxygen vacancies and good to photocatalytic performance [11].

In addition, BMO has an internal electric field induced by non-uniform charge distribution between layers. And this field favors the photo-generated e^-/h^+ pairs separation [12]. However, the photo-induced e^-/h^+ pair generation, separation, and consumption still are not ideal for advanced photocatalytic requirements. Recently, researchers have found that the noble metal was effective for photocatalytic experiments [12, 13]. On one hand, noble metal acts as efficient electron trap and capture photo-generated electrons due to Schottky barriers, facilitating the e^--h^+ pair separation [11]. On the other hand, under visible light irradiation, electrons on noble metal surface undergo collective oscillation, featuring with a strong (SPR) effect which significantly prevent e^-/h^+ pairs recombination [11-13]. Therefore, noble metal not only increases the photo-absorption, charge transfer/separation, but also promote charge consumption [13].

Another attempt is to couple optical nonlinearities with photo-catalyst in one system. The combination of nonlinear/photocatalytic mechanisms [14] will arouse interesting features to both properties. The first study on photocatalytic and nonlinear behavior in BMO/PANI [14] and in ternary $Bi_2O_2CO_3$/polypyrrole/g-C_3N_4 composites revealed promising photocurrent density and photocatalytic activity. The mechanism was not clear but probably due to the high polarizability of materials [15]. Hence, further relative investigations are necessary. At the same time, the fast development of laser technology demands materials having good nonlinearity [16]. The quantum and dielectric confinement effects in semiconductors are attractive to obtain high nonlinear property.

In addition, $Au/Co_3O_4/Bi_2MoO_6$ has another functionalized property, that is the magnetization. The highly anisotropic layered BMO structure having Bi^{3+} $6s^2$ lone pairs and distorted MnO_6 octahedral unit can yield highly anisotropic magnetic properties and ferroelectric polarization [17, 18]. Generally, it is difficult to separate the recovery the photo-catalysts during synthesis and practical application. For example, attempt to dope $ZnFe_2O_4$ into Bi_2MoO_6 to improve magnetically separation of phosphors [19]. The magnetic property can provide easy pathway for sample separation and recovery. Magnetic Co ions can compensate the nonmagnetic Mo^{6+} cations, strengthen the conjunction with the $6s^2$ lone pairs of Bi^{3+} and present stronger magnetic behavior.

In this work, we propose to couple the layered BMO with Co_3O_4 and Au nanoparticle (NPs) to form $Au/Co_3O_4/Bi_2MoO_6$ composites. This objective of this study is to utilize Co_3O_4 to provide more charge carriers and room-temperature ferromagnetism. At the same time, we utilize the high polarizability and SPR effect of Au to enhance the photocatalytic efficiency and sample separation. The possible mechanism behind nonlinearity, photocatalysis and magnetism were thoroughly studied using various techniques and DFT simulations.

2. Experiments

2.1 Synthesis of Co_3O_4/Bi_2MoO_6 composites

Bi_2MoO_6 was hydrothermally synthesized using 0.05 mol $Bi(NO_3)_3 \cdot 5H_2O$, 0.05 mol $Na_2MoO_4 \cdot 2H_2O$ and 0.26 g CTAB as precursors. After thoroughly dissolving in 30 ml ethylene glycol (EG) and 30 min- magnetic stirring, we obtained the transparent solution. Then the solution was heated to 160 °C for 12 hours and let the solution to naturally cool down to room temperature. Finally, we washed the solution with DI water and ethanol for several times to remove impurities, dried the products (BMO) at 80 °C for 6 hours. Subsequently, we ultrasonically dispersed BMO powder into 50 ml anhydrous ethanol to form BMO suspension, then we successively added $Co(NO_3)_2 \cdot 6H_2O$ and NH_4HCO_3 into suspension followed with stirring for 6 hours at room temperature, finally the precipitate was collected and calcined in air at 400 °C for 2 hours to form Co_3O_4/Bi_2MoO_6 composite.

2.2 Synthesis of $Au/Co_3O_4/Bi_2MoO_6$ composites

The $Au/Co_3O_4/Bi_2MoO_6$ catalysts were prepared by chemical reduction process. We dispersed 0.80 g Co_3O_4/BMO powder in 20 ml DI water to form suspension, and slowly dropwise added 5 ml 0.01 mol/l $HAuCl_4 \cdot 4H_2O$ and 5 ml 0.01 mol/l lysine (capping agent) into the suspension under stirring, the pH was adjusted to 5.5 through using NaOH (0.1 mol/l) solution. After ultra-sonicating the suspension for 20 seconds, we injected 5.3 ml 0.1 mol/l $NaBH_4$ to reduce the Au^{3+} to colloids Au^0. In the following time, we centrifugally washed the suspension with DI water for several times and then calcined the products at 250 °C for 2 hours to decompose residual lysine and $NaBH_4$. Bi_2MoO_6, Co_3O_4/Bi_2MoO_6 and $Au/Co_3O_4/Bi_2MoO_6$ samples were labelled as BMO, CBMO and CBMOA, respectively in this paper. In order to give a comparison, CBMO doped with various Au content of 0.1,0.2,0.3,0.4 and 0.5 mol% were synthesized as well.

2.3 Characterization, modeling and calculations

The structure of samples was examined by X-ray diffraction (XRD) using monochromatic Cu Ka radiation (λ= 1.5404 Å), Raman and FT-IR spectra. The morphology, composition, specific surface and pore volume were analyzed by Scanning electron microscopic (SEM), Transition electron microscopy (TEM), energy dispersive spectrum (EDX), and Brunauer–Emmett–Teller (BET), respectively. The optical absorption and degradation of organic pollutants were recorded on a Cary 5000 UV-visible-near-infrared spectroscopy (UV-Vis). X-ray photoelectron spectroscopy (XPS) was recorded using monochromatic Al Ka radiation to provide informaiton about chemical valences of Co, Au etc. All binding energies were calibrated using the C 1s peak at 284.8 eV of carbon.

The nonlinear absorption coefficient was investigated using Z-scan technique, using linearly polarized 4 ns pulsed Nd:YAG laser of 532 nm with a repetition rate of 2 Hz. Samples were dispersed in dimethylsulfoxide (DMSO) in a quartz cell of 2 mm thickness at the same concentration. The magnetic properties were evaluated using vibration sample magnetometer (VSM) and X-band electron paramagnetic resonance (EPR). Signals of active radicals trapped by

5,5-dimethyl-pyridine-N-oxide (DMPO) were collected at 77 K under the 781 W power and 9.604 GHz microwave frequency.

Photocatalytic performance was measured on both Methly orange and colorless pollutant using a 500 W/m^2 Xe lamp as the visible light source. Co_3O_4 and Au/Co_3O_4 also were synthesized and used as reference to CBMOA. We also did the dark experiments to extract the influence of adsorption of materials. Photocurrent density and electrochemical impedance spectra (EIS) were conducted using an electrochemical analyzer through a standard three-electrode configuration. Silver wire and saturated calomel electrodes were used as the counter and reference electrodes, respectively.

Modeling of crystal structure (Fig.1) and energy band gap of samples was simulated and calculated based on density functional theory (DFT). All calculations were based on plane wave pseudo-potential method using the Cambridge Serial Total Energy Package (CASTEP) code. Energy band structure and density of states were simulated and calculated using DFT plane-wave pseudopotential method, which can be performed to the first-principles quantum mechanics.

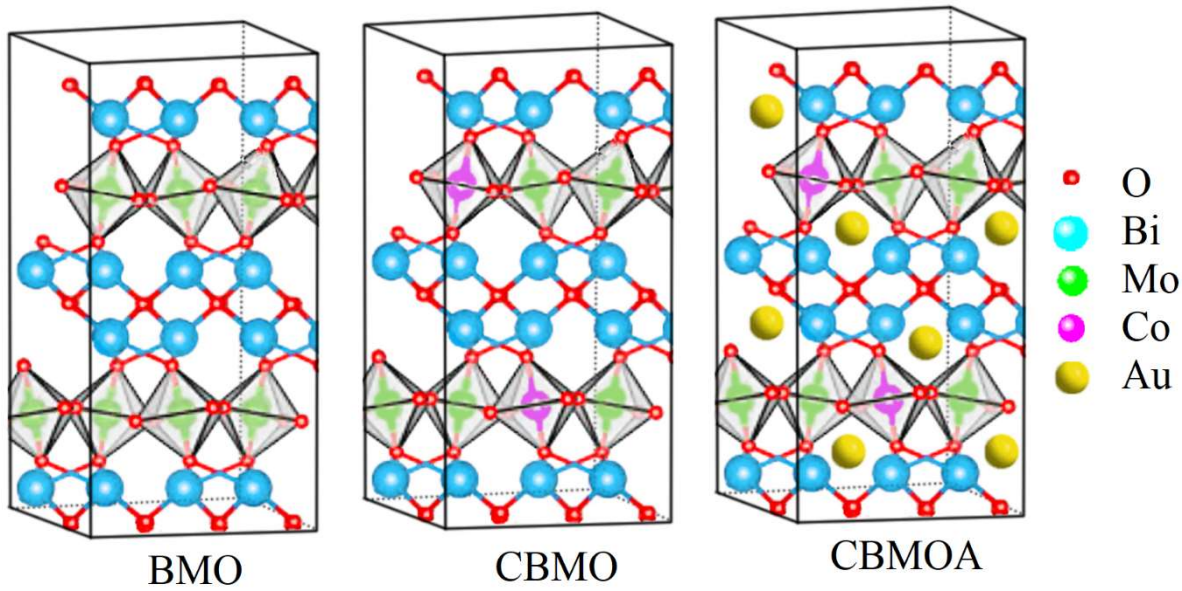

Fig. 1- Modeling structure of (a) BMO, (b)CBMO (c) CBMOA

3. Results and Discussions

3.1 Morphology, structure and chemical valence states

The morphology and microstructure of the BMO, CBMO and CBMOA are shown in Fig.2. Around 3 μm- hierarchical micro-sphere BMO was composed of a large amount of aggregated 50 nm- sheets. Fig.2c and 2d reveal that Co_3O_4 doping did not change the original structure of BMO. But small pieces were observed on surface, indicating a hetero-structure formed between Co_3O_4

and Bi_2MoO_6. In Fig. 2e and 2f, CBMOA presented very similar morphology to BMO, however with some spherical clusters on the surface.

TEM analysis in Fig.3a-3c confirms the hierarchical structure of BMO microspheres, and the lattice spacing is of 0.314 nm, corresponding to the (131) crystal plane [20]. In Figs.3d - 3f, CBMO also displays hetero-structure but with lattice spacing of 0.145 nm and 0.315 nm, respectively, corresponding to crystal plane of (440) and (131) of Co_3O_4 ad BMO [8]. For CBMOA in Figs.3h - 3j, we can clearly see that Au NPs and Co_3O_4 were located on the surface of BMO, and lattice fringe spacing was 0.226 nm and 0.244 nm, matching well to the crystal plane of (111) of Au and (311) of Co_3O_4, respectively [14].

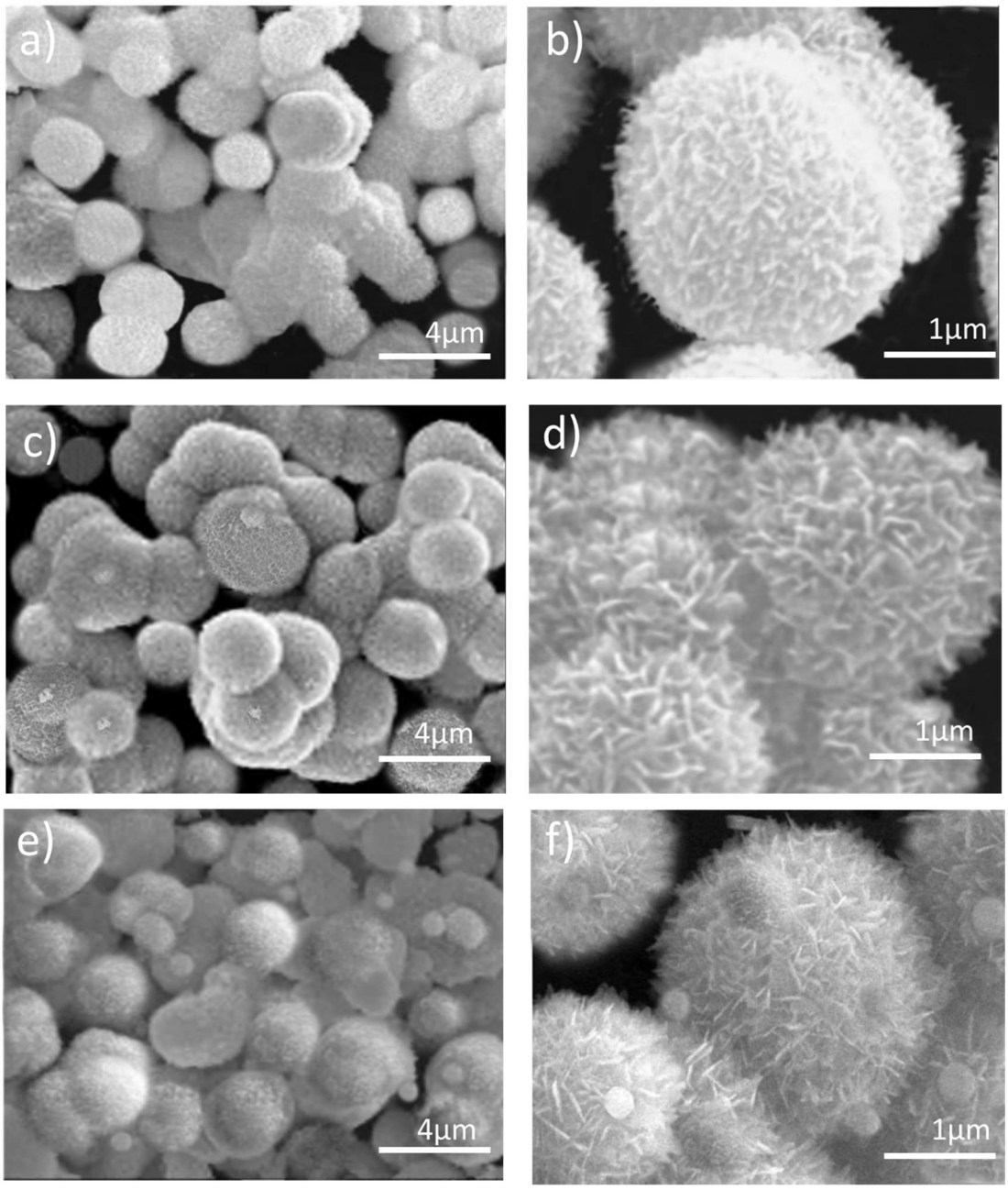

Fig.2- SEM images of as-prepared BMO (a, b), CBMO (c, d) and CMBOA (e, f) samples.

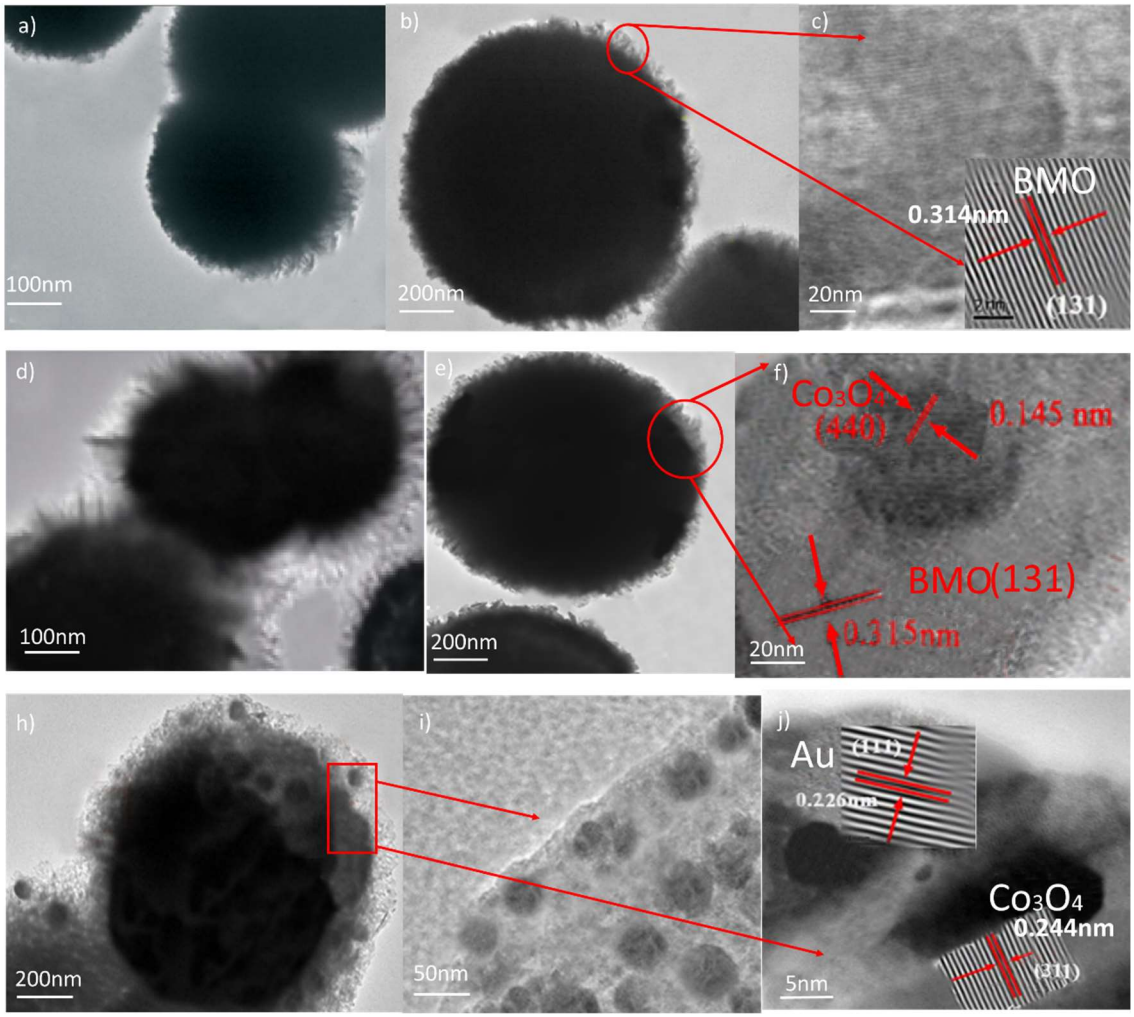

.

Fig.3- TEM images of BMO (a-c), CBMO (d-f) and CBMOA (h-j) samples, the amplified lattice spacing was put as inset.

The nitrogen adsorption/desorption isotherm curves of BMO, CBMO and CBMOA are shown in Fig.4a, 4b and 4c, respectively. Obviously, all samples belong to the type IV behavior [20]. However, slight differences of hysteresis loops still existed. BMO displays two hysteresis loops between 0.4 - 0.7 and 0.8 - 1.0 P/P_0 due to finer intra-aggregated pore [21, 22]. While the CBMO exhibits relative weak hysteresis loop at 0.4- 0.7 P/P_0. The CBMOA has no hysteresis loop at all in the same range. The specific surface area has been calculated. Compared with the value of BMO (30.60 m^2/g), the specific surface area values of CBMO and CBMOA apparently are much higher, i.e. 42.82 m^2/g and 83.64 m^2/g, respectively. Meanwhile, the pore volume values of CBMO and CBMOA increased from 0.13 cm^2/g (BMO) to 0.16 cm^2/g and 0.17 cm^2/g, respectively, indicating a stronger capability to contact with pollutants [23].

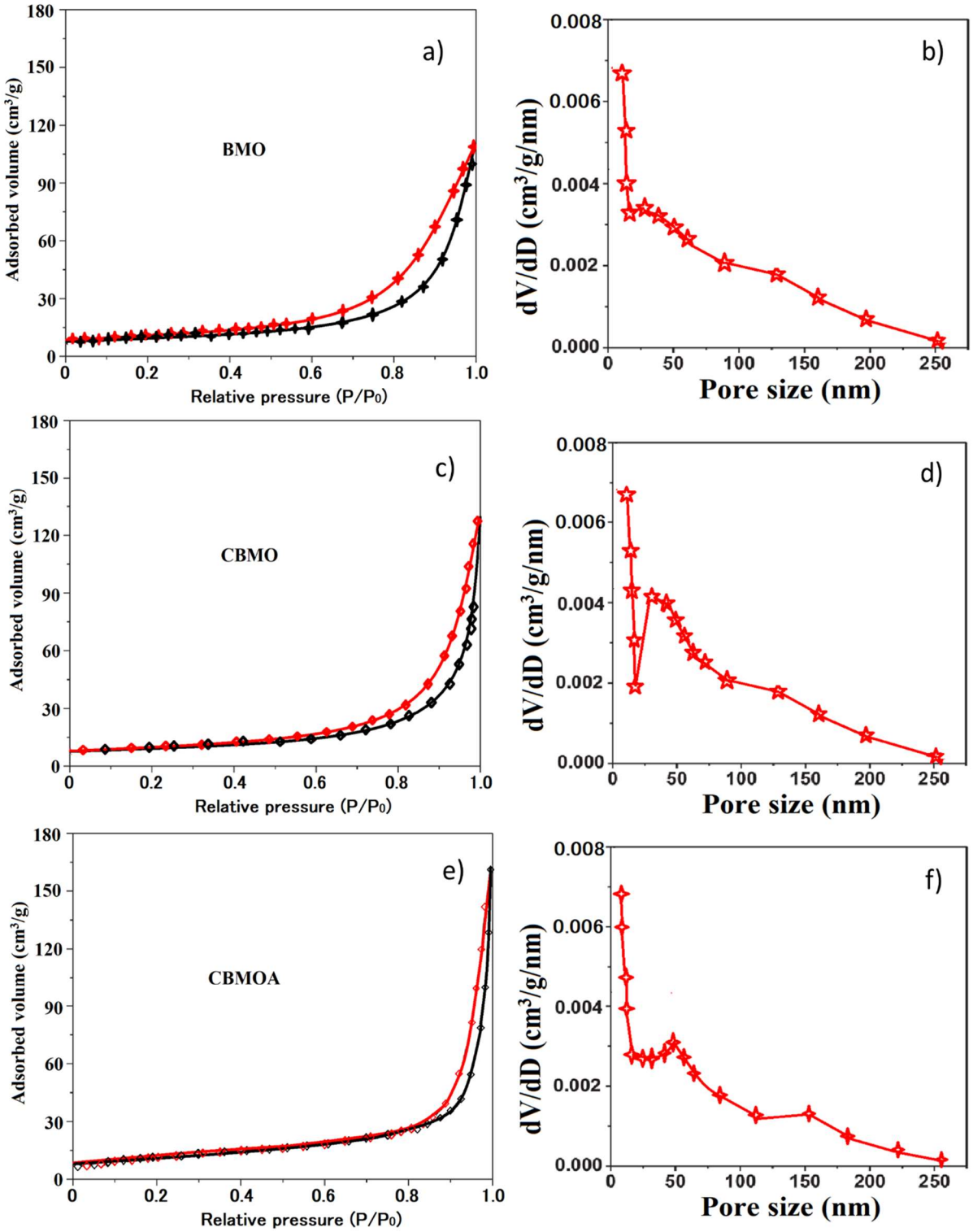

Fig.4- Nitrogen absorption–desorption isotherms and pore volume of BMO (a, b), CBMO (c, d) and CBMOA (e, f) samples, respectively.

EDX analysis of samples is shown in Fig.5. In Fig.5a, 5b and 5c, elements of Bi, Mo, O and Co and Au have been detected, and their atomic percentages agree well with the original stoichiometry compositions of Bi_2MoO_6, $Co_{0.5}Bi_{1.5}MoO_6$ and $Au_{0.3}/Co_{0.5}Bi_{1.5}MoO_6$. The appearance of Co and Au elements evidenced that the Co_3O_4 and Au has entered into BMO lattice. In order to check the distribution of each element, the element mapping of CBMOA is shown in Fig.5. We notice that the O, Bi, Mo, Au and Co elements are well distributed in the region, confirming once again the coexistence of Au and Co_3O_4 in Bi_2MoO_6. The light color of Co and Au indicates the relative smaller content in this composite.

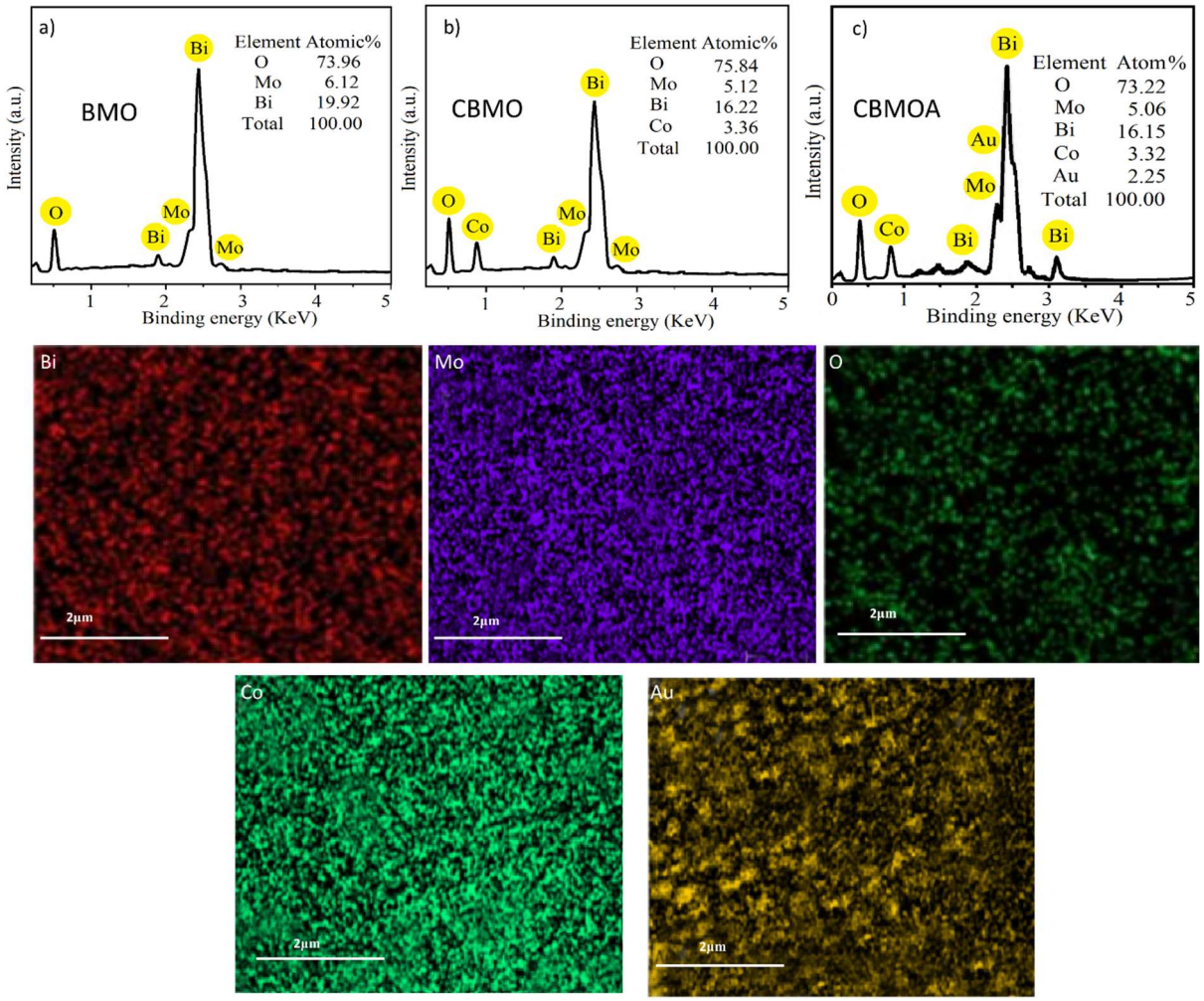

Fig. 5- SEM-EDS analysis of BMO (a), CBMO (b) and CBMOA (c), and elemental mapping images of Bi, Mo, O, Co and Au in CBMOA.

The XRD patterns of samples are shown in Fig.6a and 6b. Sharp and strong diffraction peaks at $2\theta = 28.2°$, 32.3 °, 46.9 °, 55.4 ° and 58.6 ° were observed in Bi_2MoO_6. These peaks were indexed to the (131), (022), (151), (260), (133) and (262) crystal planes of pure orthorhombic Bi_2MoO_6 [24]. The calculated cell parameters (a = 5.51 Å, b = 16.21 Å, and c = 5.49 Å) are in good

agreement with those of JCPDS No. 21–0102 [25]. CBMO and CBMOA showed almost the same XRD pattern and the characteristic peaks of Co_3O_4 were not detected. The lattice parameters of CBMOA (a = 5.511 Å, b =16.223 Å, c = 5.49 Å) are very close to that of BMO, indicating that the doping of Co_3O_4 and Au did not significantly alter the structure. Diffraction peaks of CMBOA at 38.2 ° and 44.5 ° were indexed to be the (111) and (200) planes of cubic Au [14]. From Fig.6b, we notice the (131) peak slightly shifted to larger angle side due to the introduction of Co_3O_4 and Au.

The structure was further investigated by Raman spectroscopy as shown in Fig. 6c. Similar to literature [25], the pure BMO in this study exhibited characteristic bands at 140, 197, 284, 323, 351, 716, 799 and 842 cm^{-1}. Due to lattice and E_g bending modes, the Bi^{3+} vibration appeared at 140, 197 and 284 cm^{-1}. The E_u symmetric bending and asymmetric stretching vibration of MoO_6 octahedrons were seen at 323, 351, 398 cm^{-1} and 712 cm^{-1} respectively. The most intense vibrations at 793 cm^{-1} and 840 cm^{-1} stand for the strong A_{1g} and A_{2u} symmetric and asymmetric stretching of MoO_6 octahedrons [27], respectively.

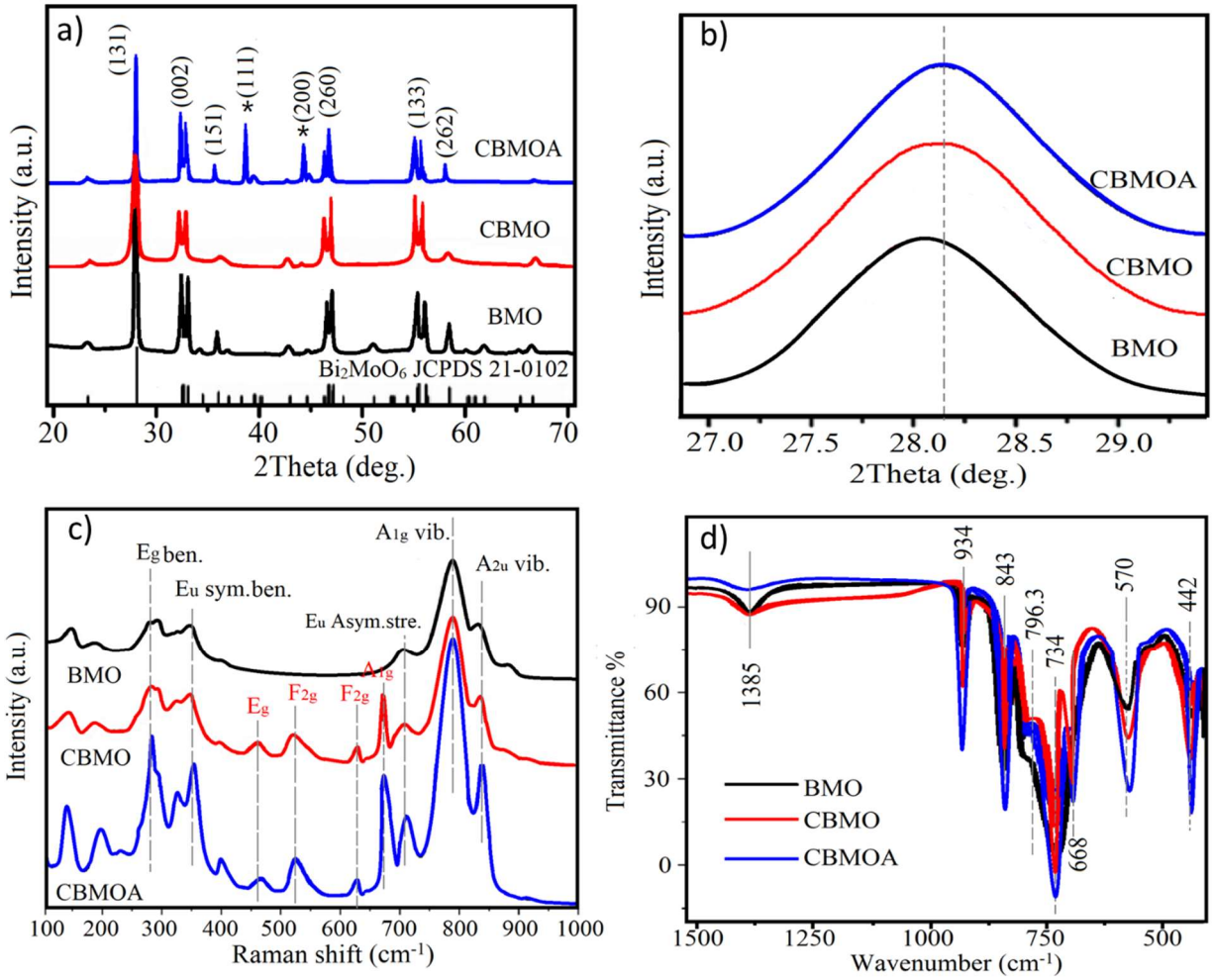

Fig.6- XRD (a, b), Raman (c) and FT-IR (d) spectra of samples

Compared to BMO, the CBMO exhibited a modification on structure as shown in Fig.6c. Co_3O_4 has tetrahedral Co^{2+} ($3d^7$) and octahedral Co^{3+} ($3d6$) two spinel configurations, and therefore Co_3O_4 presents "*Fd3m*" symmetry [28]: $\Gamma = A_{1g}$ (R) + E_g (R) +F_{1g} (IN)+3F_{2g} (R)+2A_{2u} (IN) +2E_u

(IN)+4F_{1u} (IR)+2F_{2u} (IN), where (R), (IR), and (IN) represent Raman active vibrations, infrared-active vibrations, and inactive modes, respectively [28]. In this study, CBMOA and CBMO exhibited four characteristic Co_3O_4 Raman bands at 482.2, 521.6, 618.8 and 670 cm^{-1}. These bands were indexed as the E_g, F_{2g}, F_{2g} and A_{1g} vibration modes of Co^{2+} ions, respectively. Interestingly, Raman intensity of CBMOA was significant higher than that of CBMO and BMO. And this most likely was due to surface enhanced Raman scattering effect from Au SPR [29].

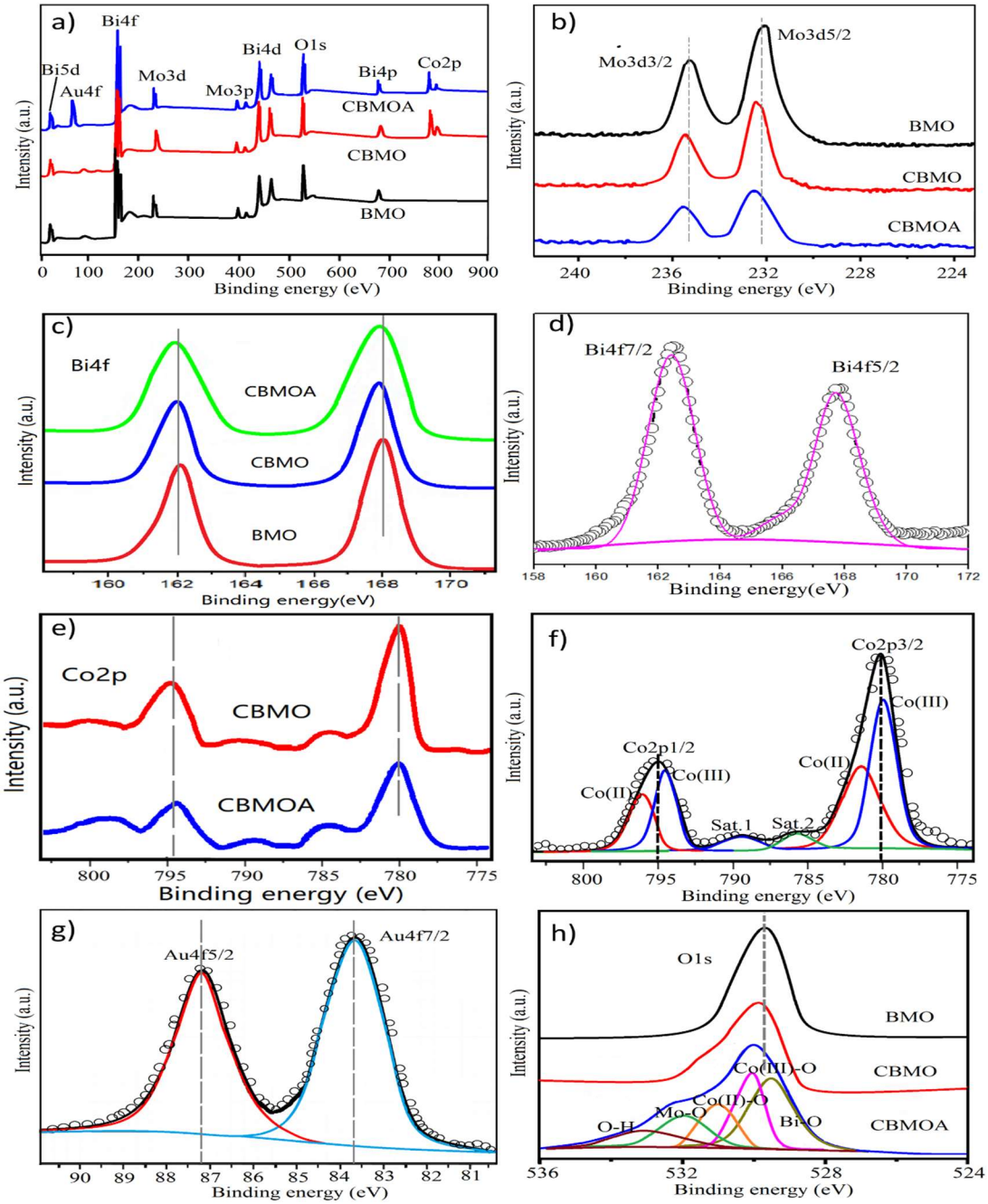

Fig.7- XPS core level energy spectra of overview (a), Mo3d(b), Bi4f (c, d), Co2p (e, f), Au4f (g) and O1s (h) of samples

The vibration modes of samples were verified by FT-IR spectra in Fig.6d. All samples had high transmittance in wavenumber > 1000 cm^{-1}. BMO in this study exhibited 7 absorption bands, among which the bands at 1385 cm^{-1} and 934 cm^{-1} were due to the bending vibration of adsorbed water and C-H bonds from organic solution (i.e. EG), respectively [27]. The asymmetric and symmetric stretching modes of MoO_6 can be seen at 843 and 796.3 cm^{-1}, respectively. The asymmetric stretching and bending vibration of MoO_6 appeared at 734 and 570 cm^{-1} [30], and at 442 cm^{-1} we notice the bending vibrations of BiO_6 [27]. Obviously, like Raman bands, the band intensities of CMBOA were remarkably stronger than others due to the SPR effect. An extra band at 668 cm^{-1} presented in CBMO and CBMOA due to the F_{1u} vibration mode of Co_3O_4. Usually Co–O stretching and O–Co–O bond bridging vibration of Co_3O_4 displays significant absorption at 567 and 661 cm^{-1} [31]. In this study, the band at 567 cm^{-1} was overlapped by strong band at 570 cm^{-1}, while the band at 661 cm^{-1} shifted to 668 cm^{-1} due to the interaction with MoO_6 which was confirmed by the slight shifts of wavenumber 570 and 442 cm^{-1}.

XPS analysis in Fig.7 can further verify the chemical valance states of Au and Co in samples. The XPS survey spectra in Fig.7a witness the presence of Bi, Mo, O, Co and Au elements, revealing the successful introduction of Co_3O_4 and Au to BMO. From Fig.7b, the characteristic peaks of Mo^{6+} centered at 232.2 and 235.8 eV shifted to higher energy side after doping of Co_3O_4 and Au [23].

The core-level energy of Bi4f of samples are shown in Fig.7c and 7d (deconvolution). A doublet of Bi 4f7/2 and Bi 4f5/2 around 162.5 and 167.8 eV verified the Bi^{3+} valence state. However, similar to that of Mo3d, compared with BMO, the binding energy of Bi4f of CBMO and CBMOA slightly shifted to longer binding energy side as well. This result indicated that the incorporation of Co ions and Au influenced the Mo3d and Bi4f through forming oxygen vacancies (OVs) [32].

The comparison of Co2p XPS spectra are shown in Fig.7e and the deconvolution of Co2p of CBMOA is shown in Fig.7f. We notice that two main peaks around 795 and 780 eV are corresponding to the Co2p1/2 and 2p3/2, respectively. Through the observation, we found the binding energy of Co2p did not shifted after Au doping, revealing the reduction process did not greatly influence the chemical state of Co ions. The deconvolution of Co2p of CBMOA in Fig.7f displays 6 peaks involving two spin–orbit doublets and two satellites. Such feature indicates the coexistence of Co^{3+} and Co^{2+} whose ratio (Co^{3+}: Co^{2+}) was calculated to be 1.998, very close to the theoretical ratio of Co^{3+}: Co^{2+} in Co_3O_4. Fig.7g shows the binding energy of Au4f in CBMOA and deconvolution curves. The fitted two peaks at 83.6 eV and 87.2 eV correspond to Au4f5/2 and 4f7/2 of metallic Au, respectively [34].

To further study the formation of OV and changes of oxygen species, O1s binding energy of three samples is shown in Fig.7h. Apparently, the O1s peak shifted to higher binding energy side after the introduction of Co-O bonds in BMO. On the other hand, O1s peak of BMO is symmetric, while that of CBMO and CBMOA are asymmetric, indicating the production of oxygen defects or vacancies. From the deconvolution of O1s of CBMOA, 6 peaks corresponding to the lattice oxygen of Bi-O, Co^{3+}–O, Co^{2+}–O, Mo-O and O-H bonds were observed at 529.4, 530, 531.1, 532 and 533.1 eV, respectively. This observation not only indicated that the successful incorporation of Co_3O_4, but also verified the production of OVs in CMBOA sample. And the OVs are helpful to photo-catalysis activities.

3.2 Photocatalytic activity

The optical absorption spectrum of MO shown in Fig.8a presents distinctly reduction of intensity in the order of CBM>CBMO>CBMOA than that in dark. For the same irradiation time period, CBMOA exhibited apparently lower absorption intensity of MO, suggesting that the MO was almost totally decomposed after irradiation 1 hour. The much superior photocatalytic activity of CBMOA may be attributed to the synergistic effect from both Au SPR and Co_3O_4. Such synergistic effect not only improved the visible light response ability, but also combined the strong SPR effect with active electron transition and charge transfer from Co_3O_4, promoting the efficient separation of photo-generated electron-hole pairs. In order to further verify the photocatalytic activity, CBMO doped with different Au contents from 0.1 to 0.5 mol% were subjected to photo-degradation test. As shown in Fig.8a and 8c, the photo-degradation of MO increased with the Au content. We also performed the photocatalytic activity test of Co_3O_4 and Au&Co_3O_4 to compare with other samples. As shown in Fig.8a, the degradation activity of Co_3O_4 was smaller than CBMO and Au&Co_3O_4, and the CBMOA presented the best performance. This result revealed that the Co ions and Au have provided easy and efficient pathway to deliver electrons for photo-catalysis.

MO concentration as a function of irradiation time was shown in Fig.8b and 8c. The photo-degradation efficiency (Ƞ%) of MO was estimated using Eq. (1)

$$\eta = \frac{C_0 - C}{C_0} \times 100\% \quad (1)$$

Where C_0 refers to the original concentration (20 mg/l), C is the concentration after visible light irradiation. Obviously, BMO, CBMO and CBMOA has decomposed about 22 %, 48 % and even 97.2 % of MO, respectively. The kinetic behaviors were investigated through plotting $\ln(C_0/C)$ as function of irradiation time and shown in Fig.8d. Clearly, all of them fit well with the pseudo-first-order kinetics model [35]: $\ln(C_0/C) = k_{app}.t$, where k_{app} denotes the apparent rate constant and t is irradiation time. Fig.8d reveals an almost linear fitting to data for all samples, indicating they followed the pseudo-first-order kinetics mode. Particularly, CBMOA exhibited the highest k_{app} value of 135×10^{-4} min^{-1}, which is 5.86 times higher than that of pure BMO. Au NPs and Co ions in CBMOA worked as electrons-captor, and the large specific surface area provided more active sites which efficiently prevented the recombination of e^-/h^+.

Photocatalytic stability in Fig.8e illustrates a very slight decrease of photocatalytic performance after 5 cycles and the XRD patterns of CBMOA after 5 cycles were almost the same to original one. These results indicated that the CBMOA was quite stable and reusable photocatalyst to degrade organic pollutants in practical applications.

Considering the possible photosensitivity of MO, a colorless pollutant (phenol) was used to further assess the actual photocatalytic activity of present samples, in order to exclude the possible contribution of photosensitization to photocatalytic activity. Fig.9 displays the photocatalytic degradation and change of concentration of phenol irradiated by 269 nm. For the performance of BMO, we notice the phenol has high absorption at 260-280 nm range after irradiated for 1 hour, then the intensity decreased after 3 hours' irradiation. Under the same irradiation time period, CMBO exhibited stronger but CMBOA the strongest degradation behaviors on phenol. The concentration changes of phenol in Fig.9b show a similar photocatalytic behavior to that of MO, confirming the good photocatalytic activity of CMBOA.

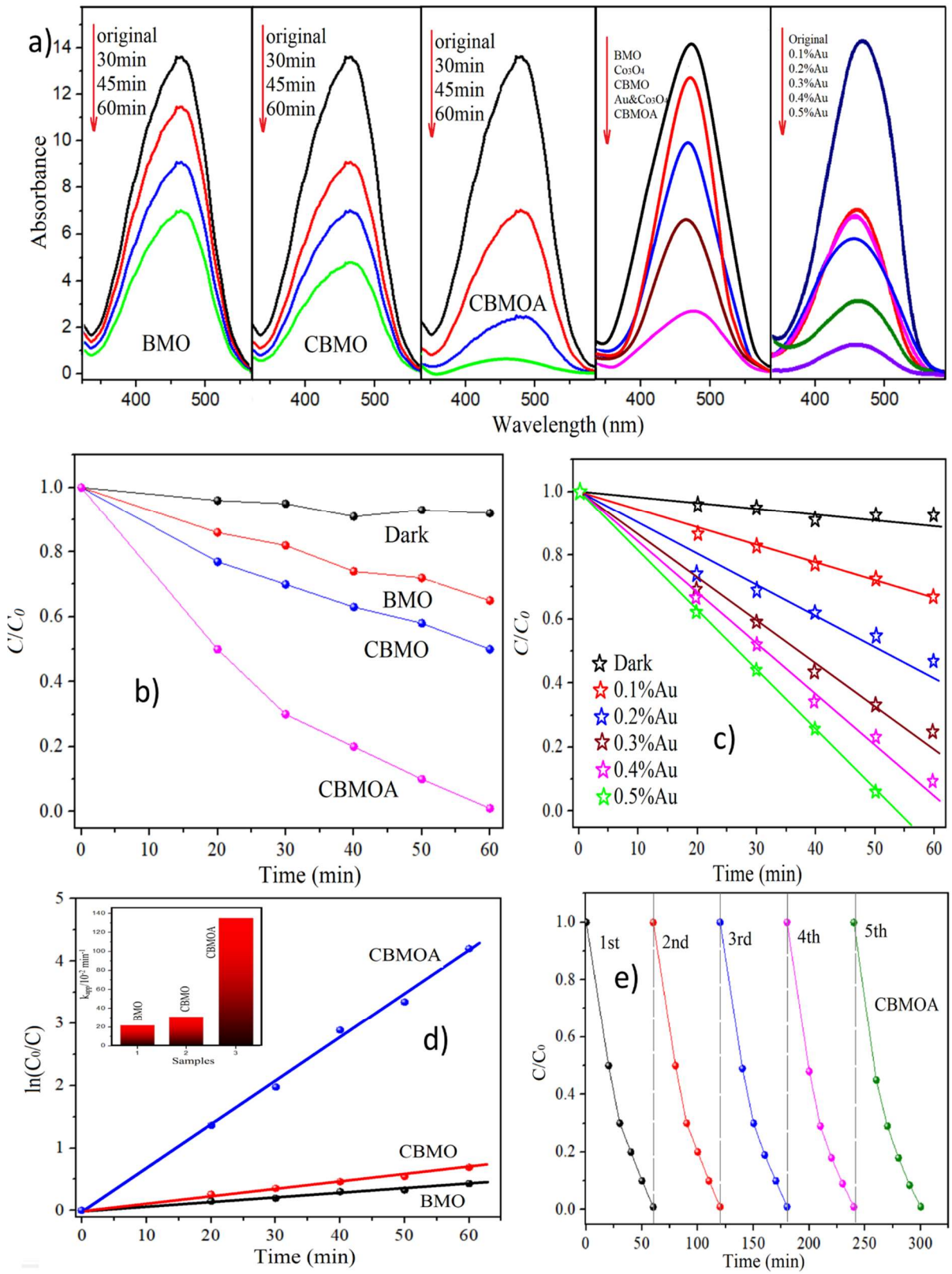

Fig.8- Degradation of MO (a), C/C_0 and $\ln(C_0/C)$ versus time curves (b, c and e) and photocatalytic stability (e) of samples

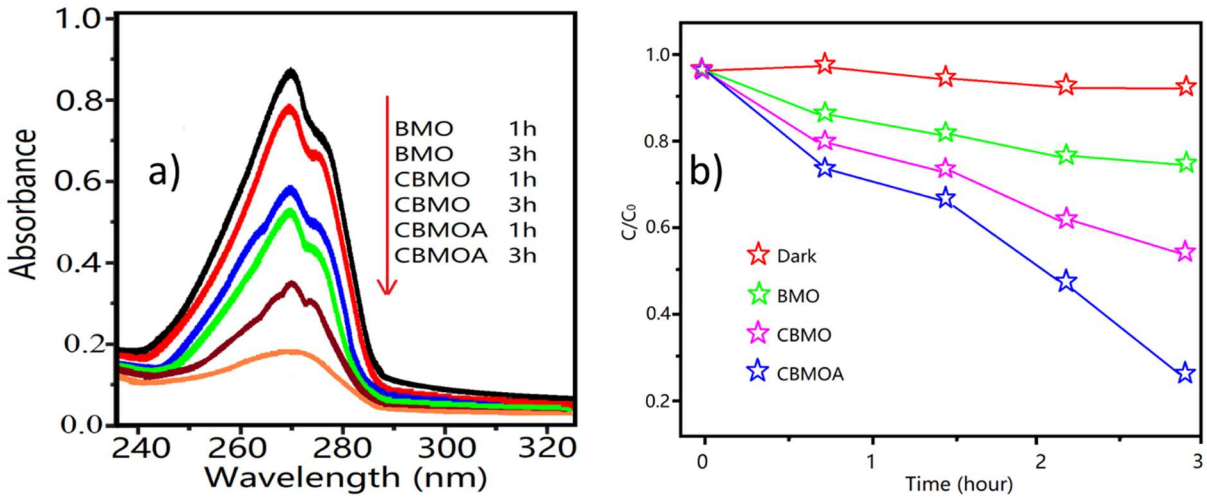

Fig.9- Photo-degradation of colorless phenol (a) and photocatalytic efficiency (b) of samples.

3.3 Photo-generated carrier behavior and thermal stability

To further evaluate the generation and transfer of photo-induced charge carriers, we conducted the photocurrent response and electrochemical impedance spectroscopy (EIS). Fig.10a reveals the CBMOA has much higher photocurrent density, i.e., 2.7 folds larger than pure BMO, revealing the Co_3O_4 and Au positively functioned for photocatalytic activity. The EIS test in Fig.8b displays the typical EIS Nyquist plots of samples: a semicircle over high frequency range followed by a linear part in low frequency range. And it is well known that a smaller the arc radius represents a lower electric charge transfer resistance and a faster electron transfer rate [36]. The significantly smaller arc radius of CBMOA than that of CBMO and BMO implied a stronger e^-/h^+ separation and transfer ability.

A resistance-constant phase element (CPE) series equivalent electrical circuit model was applied to simulate the EIS results (inset of Fig.8b). The circuit was consisting of solution resistance (R1), interfacial resistance between semiconductor electrode and electrolyte (R2), and constant phase element (CPE). The computed parameters are listed in Table 1.

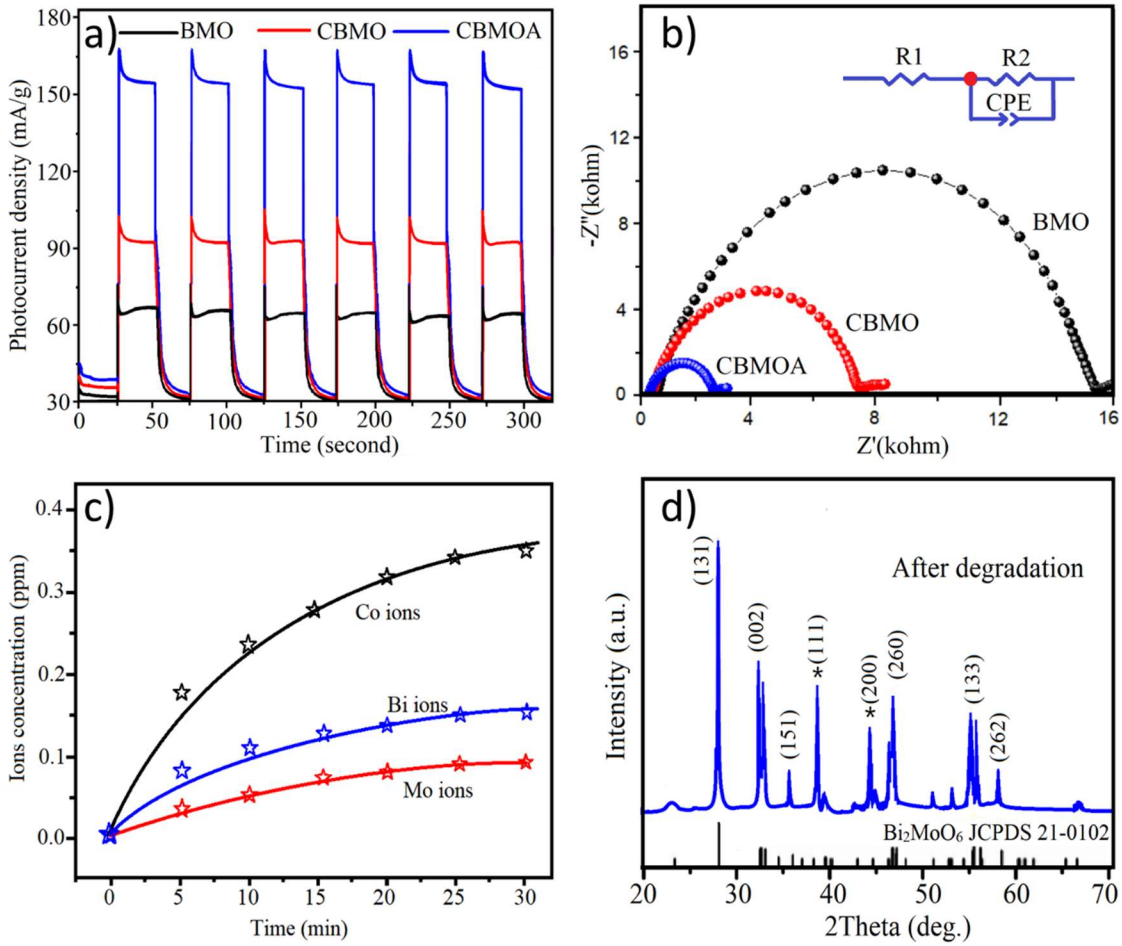

Fig.10- Transient photocurrent response under visible light irradiation (a), Electrochemical impedance spectroscopy (EIS) (b), leaching test (c) and XRD pattern after reaction(d).

Table 1- Calculation results of equivalent circuit parameters from the fitted impedance spectra

Materials	R1(Ω)	R2 (Ω)	CPE (10^{-5} F cm^{-2})
BMO	36.3	132.4	8.9
CBMO	23.4	122.8	11.5
CBMOA	8.6	84.6	28.6

The leaching test after 30 min of reaction was performed in order to further explore the stability of CBMOA. The leaching of Co, Au, Bi and Mo ions in the reaction solution was determined using ICP-OES as shown in Fig.10c. We found that as the photocatalytic process progressed, some Co, Bi and Mo ions leached from the CBMOA. However, Au ions were not detected. After 30 min, the maximum leaching concentrations of Co, Bi and Mo ions in the solution were 0.25, 0.16 and 0.1 mg/l, respectively. These values were much less than the standard level (0.5 mg/l) and also confirmed the good stability of CBMOA. In addition, the XRD pattern of CBMOA after

degradation is shown in Fig.10d. After comparing with the original XRD pattern of CBMOA, we notice that no detectable crystal peaks appeared, confirming the good stability of CBMOA.

Table 1 shows an apparent decrease of R1, R2 and an increase of CPE value on the contrary. This result suggests a faster charge transport /transfer at the interface of semiconductor and electrolyte, which efficiently restrained the charge recombination. In this study, the reason and mechanism behind the significantly photocatalytic activity of CBMOA were investigated from the point of view of optical absorption/energy band gap/SPR, DFT simulation, influence of nonlinearity and EPR OVs analysis.

3.4 Influence of optical absorption, SPR, energy band gap and DOS

Optical absorption, energy band gap and SPR effect were firstly investigated in Fig.11. Clearly, BMO exhibited a steep absorption edge at 448 nm, indicating that absorption was not originated the transition from impurity level but intrinsic band gap transition [24]. Using the Tauc' plot in Eq. (2) in Fig.11b, the indirect band gap of BMO was calculated to be 2.77 eV which is close to the value of 2.4-2.9 eV from literatures [2].

$$A = \frac{\left[k(hv - E_g)^{\frac{n}{2}}\right]}{hv} \quad (2)$$

Where A is optical absorption, k is constant = $\alpha\lambda/4\pi$, h is Planck's constant (6.626176×10^{-34} Js), v is light frequency, $n = 1$ for direct electronic transition. α is optical absorption coefficient.

As shown in Fig.11a, the visible light absorption of CBMO was significantly enhanced which favors photocatalysis activity. Also the absorption edge was not as steep as that of BMO and red shifted, demonstrating the influence of Co_3O_4. CBMO exhibited an extra broad absorption peak centered at 700 nm due to the *d-d* spin and electron-dipole allowed $^4A_2(4F) \rightarrow {}^4T_1(4F)$ transitions of tetrahedral Co^{2+} crystal symmetry [32]. The most likely reason for the obvious broadening of this band was the overlapping with the $^5T_{2g} \rightarrow {}^5E_g$ transition of Co^{3+} ions. Another $^5E \rightarrow {}^5T_2$ transition of Co^{3+} ions at 430 nm was completely covered by the strong absorption edge of CBMO in the same spectra range.

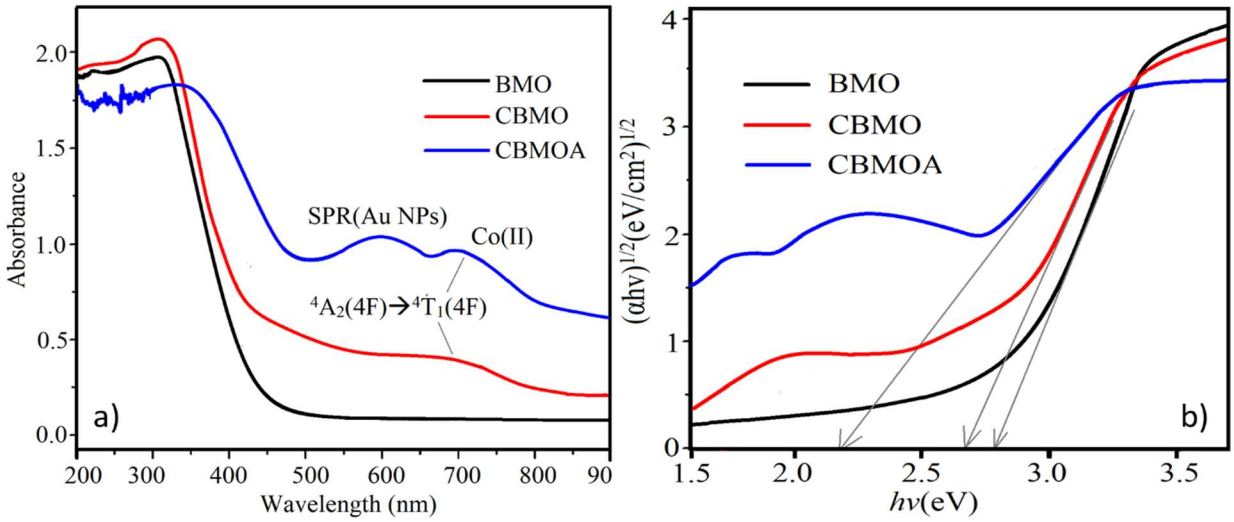

Fig.11- Optical absorption spectra (a) and Tauc's plot (b) samples

From Fig.11a, among the absorption edges of three samples, the absorption edge of CBMOA shifted to the longest wavelength, and not as steep as that of CBMO and BMO. In addition, CBMOA presents the strongest visible light absorpiton with an intense SPR peak of Au NPs at 580-600 nm [13]. The greatly enhanced absorpiton in the visible region are plausible for photocatalysis reaction. Another important feature of CBMOA is the apparently enhanced $^4A_2(4F) \rightarrow {}^4T_1(4F)$ transitions of Co^{2+} ions around 700 nm wavelength, which is much stronger than CBMO, verifying that the oscillation of electrons of Au SPR effect produced a strong electric field inside CBMOA and accelerated the electron transition of Co^{2+} ions. These promising features contributed to the excellent separation of photoexcited e^-/h^+ pairs.

The calculated band-gap energies (E_g) of CBMOA (2.12 eV) was much smaller than BMO and CBMO. All these positive factors endowed CBMOA a large harvesting capability of visible light and more actived photocatalysis capability.

3.5 DFT simulated electron structure and DOS

The electron structure and density of states (DOS) were further simulated using DFT method to determine the contribution of the atomic orbitals to the electronic structure. As shown in Fig.12a, 12b and 12c, the simulated E_g is 2.72 eV, 1.84 eV and 2.12 eV for BMO, CBMO and CBMOA, respectively. The DOS provided the probably contribution from element orbits to E_g.

From Fig.12d, one can see that the valence band and conduction band are composed of the hybrid orbital of O2p, Bi6s and Mo4d orbitals. All of them have contributed to the visible light absorption [38]. Among these orbitals, oxygen atoms with O2p orbital are the main contribution to states below the Fermi energy, while the minimum of conduction states (from 0.0 to 5.0 eV) dominantly relied on the contributions of [Mo]4d and [O]2p orbitals [37]. The electron numbers near the Fermi energy reached to 27 eV.

In Fig.12e, we notice that an obvious new sharp and intense Co3d orbital gave a much bigger contribution to the valence band states of CBMO than that of O2p, Bi6s and Mo4d orbitals. The conduction band state of CBMO came mainly from O2p orbital which provided significantly sharp and intense peaks. Fig.8e revealed that the introduction of Co_3O_4 decreased the E_g and increased the electron numbers near Fermi energy to 38 eV which is promising for photo-catalyst activity. On the other hand, the significantly intense peak of O2p also implied the formation of OVs with defect level which might favor the electron excitation and e^-/h^+ separation in CBMO.

The DOS of CBMOA in Fig.12f displays the best photocatalysis behavior among three samples. Firstly, the significant oscillation of electrons on surface of Au NPs gave strong peaks which increased the electron numbers to 70 eV which is double higher than that of pure BMO. Secondly, the SPR effect on Au surface enhanced the activation of O2p and Co3d electrons, which gave important contribution to the decrease of energy band and photo-catalysis reaction. Finally, appearance of Bi6p orbital in CBMOA confirmed once again the formation of OVs which benefited to the photo-excited e^-/h^+ separation in CBMOA.

Through the electron structure and DOS results of BMO and CBMOA, it can be concluded that their main differences are the three peaks (Au, Co3d and O2p orbitals) around the Fermi energy level in DOS which remarkably activated the interactions between O atoms with surrounding Co and Au atom.

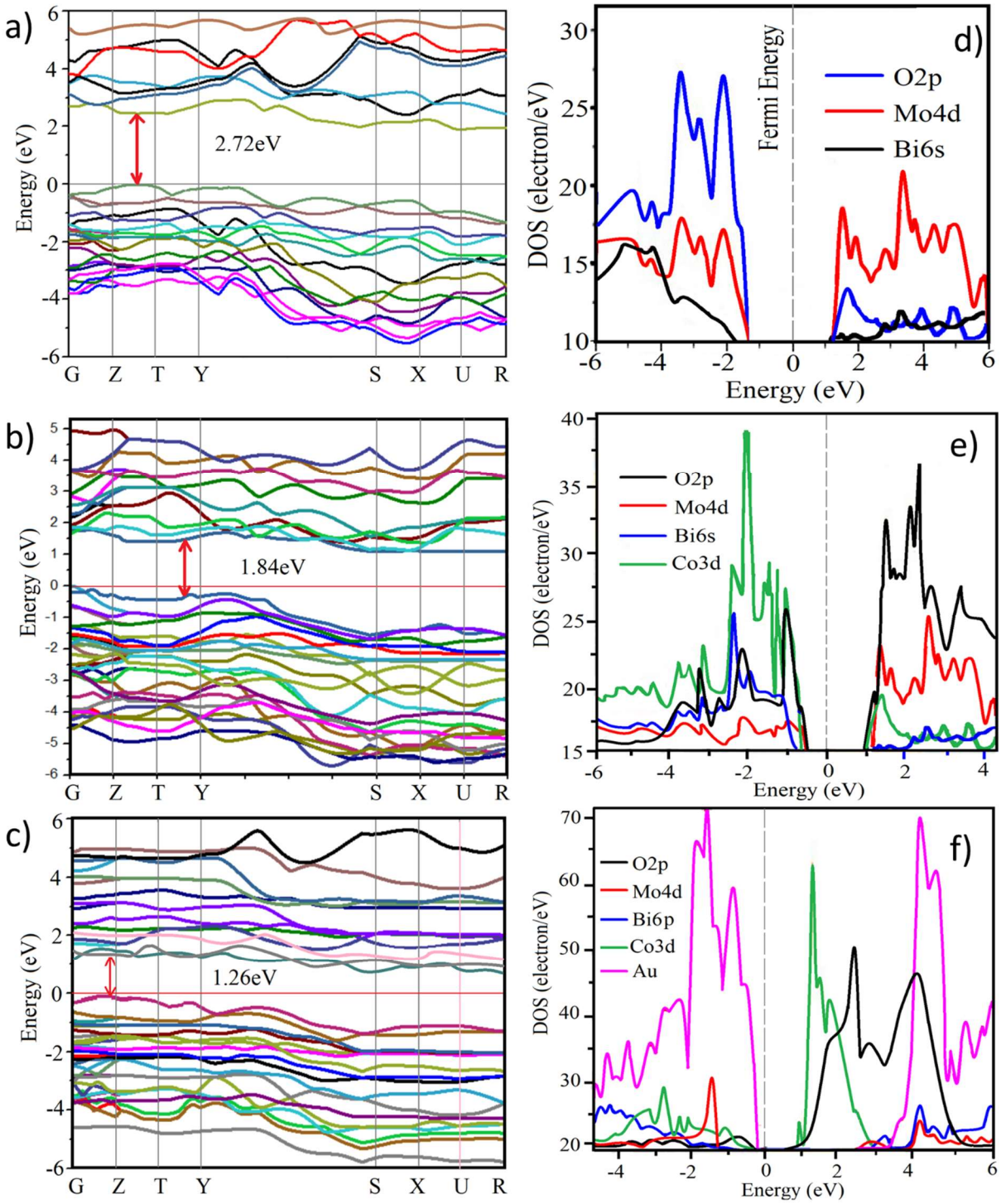

Fig.12- DFT simulation of energy band gap (a-c) and DOS (d-f) of BMO, CBMO and CBMOA samples, respectively.

3.6 Influence of nonlinear absorption

Efficient electron transition and charge transfer of CBMOA is advantageous for optical limiting applications. Possible mutual influence between nonlinearity to photocatalytic activity was investigate using Z-scan technique. Fig.13a displays the open aperture Z-scan of three samples. It is evident that CBMOA displayed a much deeper valley and positive nonlinear absorption of incident light with a typical absorption saturation, indicating a superior optical limiting behavior [14-16]. As a comparison, CBMO displayed much weaker nonlinearity while pure BMO almost no obvious signal. This observation suggested the strengthening of third-order nonlinearity mainly ascribed to the Au NPs. The closed-aperture Z-scan curves in Fig.13b illustrates a positive nonlinearity and self-focusing behavior of three samples.

We have obtained the value of nonlinear absorption coefficients α_3 through fitting the normalized transmittance curve of closed-aperture Z scan according to expression in Eq. (3), the power density used here was $I_0 = 0.90$ GW/cm^2.

$$\Delta T_{OA} = 1 + \frac{\alpha_3 {I_0}^2 L}{3^{3/2}\left[1+\left(\frac{Z}{Z0}\right)^2\right]^2} \quad (3)$$

where T_{OA} represents the normalized transmittance difference between peak and valley, α_3 stands for the nonlinear absorption coefficient, I_0 is the peak intensity at the focus (z=0), L is the thickness (1.5 mm) of cuvette. We notice that a much stronger nonlinear absorption coefficient was obtained for CBMOA (Table 2) due to hetero-structure with diverse chemical compositions.

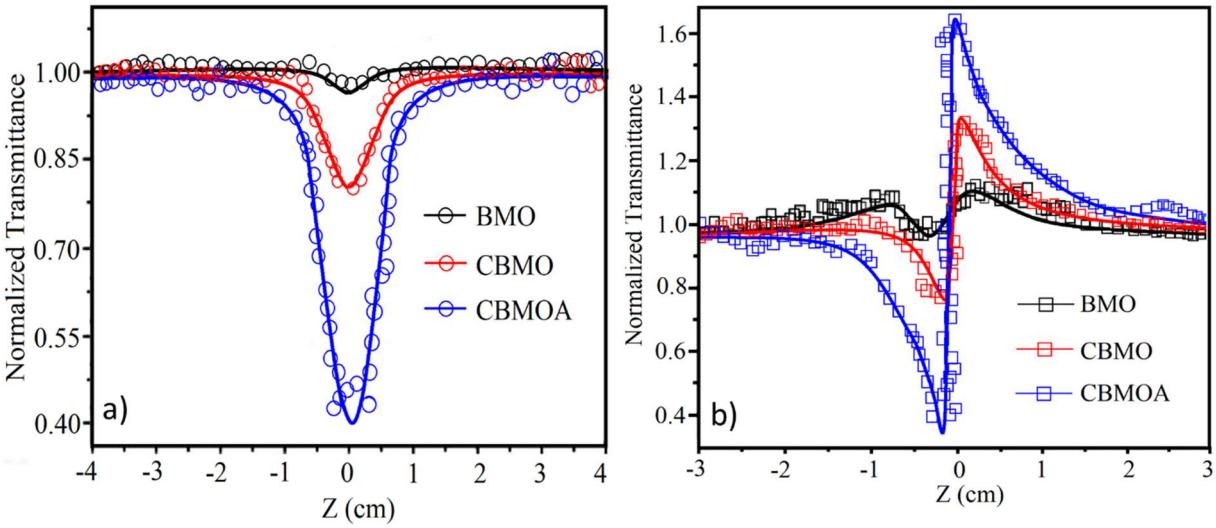

Fig.13- Open-aperture (a) and closed-aperture (b) Z-scan curves of samples.

It is well known that the nonlinearity originates from the non-centrosymmetric structure of material [14]. In this study, the doping of highly polarized Au NPs increased the polarizability of CBMOA, and thus seriously broke the Centro-symmetry of structure. From previous DFT and DOS studies, we have known that the introduction of Co_3O_4 has greatly increased the electron transitions and charge transfer, therefore, the increase of polarizability efficiently paved an easy pathway for these

electron transitions and charge transfer, resulting in the final improvement of photocatalytic performance. The nonlinearity study promotes us to conclude that, the doping of Au greatly increased the disorder and polarizability of structure, which not only good to nonlinear optical properties, but also significantly benefit to superior photocatalytic activities.

3.7 EPR spin trapping of active radicals and OVs

The active-species trapping experiments are important and are reported in Fig.14 to reveal the main radicals responsible for pollutant degradation and reasons behind high photocatalytic activity of CBMOA. In this study, through the trapping test, the main radicals responsible for pollutant degradation were mainly the .OH, O_2^- and OVs. The spin trapping agent DMPO and photo-generated holes produced the radical cation $DMPO^+$, which subsequently reacted with water molecules and formed spin-adduct DMPO-•OH [39]. However, it is obvious that the radical signals were very weak in dark. From Fig.14a, typical four-line EPR signals with an intensity ratio of 1:2:2:1, assigned to characteristic peaks of DMPO-•OH spin-adduct (spin Hamiltonian parameters g = 2.0057), were generated in all samples after irradiation [36]. However, CBMOA displayed distinct higher signal intensity, implying Co species and Au remarkably accelerated the ability to producing •OH radicals. Fig.14b shows the EPR spin trapping signal of superoxide radical DMPO-$•O^{2-}$. After visible light irradiation, electrons on the conduction band (CB) of BMO (-0.38 V) reduced O_2 to $O_2^{\cdot-}$ (-0.046 V for $O_2/O_2^{\cdot-}$ potential), and presented characteristic quartet peaks of DMPO.O_2^- adduct (g=2.009) with intensities of 1:1:1:1, due to the hyperfine coupling of superoxide ion with I=5/2 spin of the ^{17}O nucleus [40]. From Fig.10b, CBMOA presented the strongest DMPO.O_2^- signals for the same reason. The greatly enhanced radical signals explained the reason for high photocatalytic activity of CBMOA in Fig.7 and Fig.8.

Besides $O_2^{\cdot-}$ and •OH radicals, the OVs also played important role for photo-degradation reaction. To further verity the formation of OVs and monitor the behaviors of OVs, EPR spectra of three samples were conducted and shown in Fig.14c. It is known that ^{59}Co has I=7/2 which gives rise to a hyperfine patter when we apply the magnetic field. Among Co ions, diamagnetic Co^{3+} ions from Co_3O_4 ($3d^6$ configuration) are EPR silent, while Co^{2+} ($3d^7$ configuration) ions are EPR active. Moreover, EPR study mainly demonstrates the information of Co^{2+} ions. Generally, the spectra of tetrahedral coordinated Co^{2+} are composed of one dominant sharp peak and one weaker but relatively broad peak [35]. Also the EPR signal of Co^{2+} strongly depends on concentration, spin states and coordination environment. In this study, the BMO showed a weak EPR signal at g = 2.001 due to the formation of OVs. Similar EPR signals were reported for pure BMO at g= 1.991 - 2.004, depending on the synthesis conditions and number of OVs. No other EPR resonance signal in the magnetic field was detected in BMO.

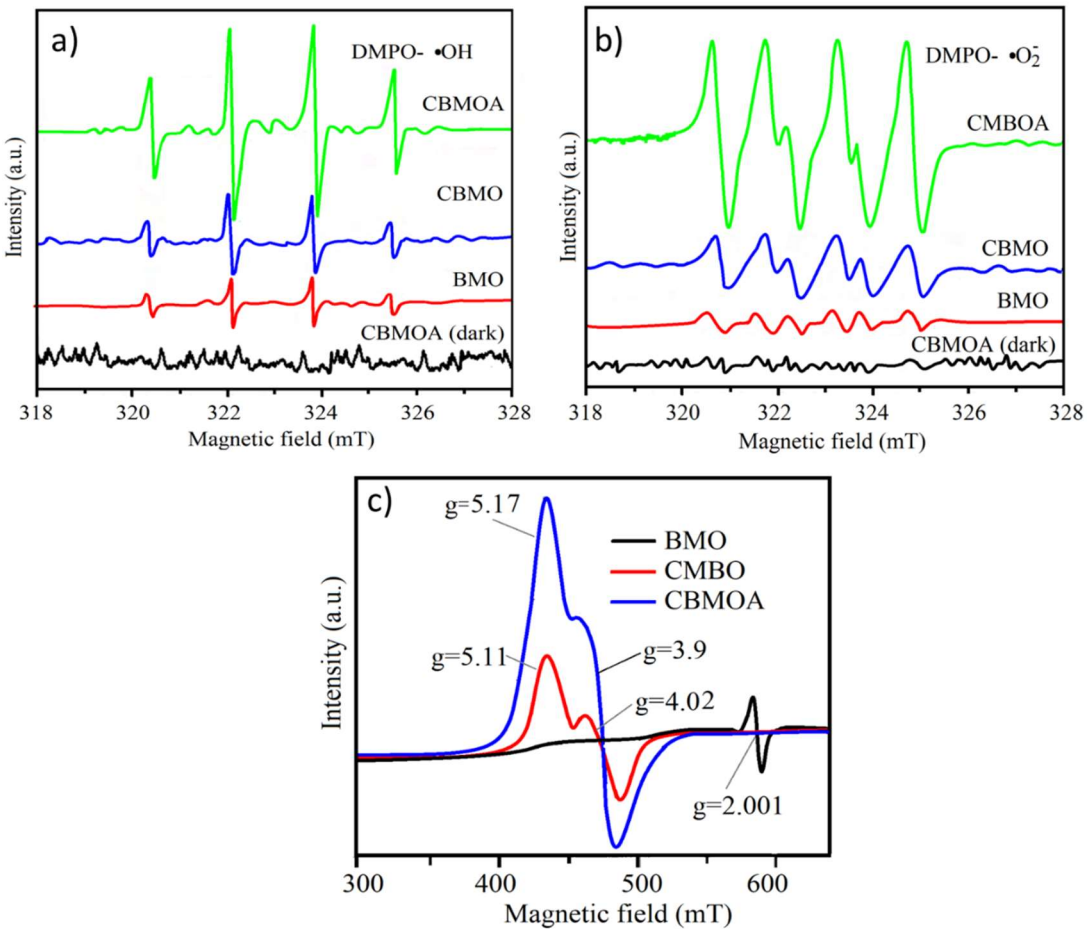

Fig.14- EPR DMPO-O_2^- (a), DMPO-.OH (b) and EPR spectra (c) of samples.

Contrary to BMO, CBMO (CBMOA) exhibited an obvious axial-type EPR signal of Co^{2+} spin centered around g=5, which consisted of one much stronger peak at g=5.11 (5.17) and another weaker one at g=4.02 (3.9). This confirmed the Co^{2+} ions existed as extra active species to photocatalytic performance [40].

There are two distinct features can be noticed from Fig.14c. Firstly, the intensity of EPR of CBMOA was significantly higher than that of CBMO. From XPS of Co2p analysis, the reduction process slightly reduced Co^{3+} to Co^{2+} which was not considered to be influential factor to the change of EPR. Hence the improvement of EPR signal most likely was due to spin states and coordination environment of Co^{2+} which was altered by Au SPR effect. The second feature is the broadening of EPR peak whose g value shifted from g =5.11 (CBMO) to g =5.17 (CBMOA). The g values of CBMO correspond to the M_s of S=±1/2 ground low spin state transition of Co^{2+} [35]. After decoration of Au NPs, the spin state of Co^{2+} changed to high spin state of M_s of S=±3/2, suggesting that the Au NPs altered the environment and the changed the affinity of the metal-binding site of Co^{2+} [11]. On the other hand, the reduction reagent $NaBH_4$ has strong reducing capability to active hydrogen which could easily formed the OVs. Exactly because of the unpaired electrons trapped by the OVs, the EPR signals of CBMOA was much stronger than that of CBMO.

Therefore, both the change of spin states of Co^{2+} and the formation of OVs have resulted in the strong EPR signal of CBMOA. And importantly, the formation of OVs contributed to the increase of photocatalytic efficiency.

3.8 Mott-Schottky analysis and Photocatalytic Mechanism

In order to understand the electron-hole pair separation mechanism, the flat band potentials of BMO and Co_3O_4 were determined through Mott-Schottky test. As displayed in Fig.15a and 15b, BMO showed a positive slope of the Mott-Schottky curve while the Co_3O_4 of showed a negative slope of Mott-Schottky curve, indicating they belong to n-type and p-type semiconductor, respectively. In addition, the Mott-Schottky plot in Fig.15a and 15b indicated that the flat-band potential of BMO and Co_3O_4 is approximately -0.365 V and 1.13 V, respectively. In general, the flat band positions are 0.1 ~ 0.3 eV lower than the valence band edge (VBE) and higher than the conduction band edge (CBE) of n semiconductor [36]. Moreover, the Fermi level of BMO and Co_3O_4 can be expected to be about −0.37 eV (-0.163 eV *vs*. NHE) and 1.12 V (1.32 V *vs*. NHE), respectively.

On the basis of aforementioned analyses, including SPR, DFT simulation on electron structure, DOS, energy band gap, the polarizability through nonlinearity, the active radicals and flat band voltage analysis, we conclude that the remarkable photocatalytic performance of CBMOA may be attributed to the synergistic effect of SPR of Au NPs, multivalence states of Co, OVs and the hetero-structure. Therefore, a possible mechanism describing the charge transfer and separation process was plotted in Fig.15c. The CB and VB positions were calculated according to the following empirical formulas in Eq (3) and (4) [1]:

$$E_{VB} = X - E_e + 0.5E_g \quad (3)$$

$$E_{CB} = E_{VB} - E_g \quad (4)$$

Where E_{VB} is the *VB* edge potential, X is the electronegativity of sample, which is the geometric average of the absolute electronegativeity of the constituent atoms, E_e is the band free electrons on the hydrogen scale (E_e = 4.5 eV) and E_g is the energy of gap energy of samples.

The mechanism can be interpreted in this way: Firstly, CBMOA obviously had greatly enhanced light harvesting in UV, visible to near infrared region due to Au SPR and SPR enhanced electron transition of Co ions. This capability contributed to generate more active electrons and holes on surface. Secondly, the photo-generated electrons-holes separation was facilitated through constructing p-n hetero-structure of Co_3O_4-BMO, the build-in electric field induced by SPR effect and the unbalance of electron distribution between layers of BMO. The photo-generated electrons transferred from *VB* of Co_3O_4 and Bi_2MoO_6 to corresponding *CB*, yielding photo-generated holes remained at the *VB* position ($Co_3O_4/Bi_2MoO_6 + h\nu \rightarrow e^- + h^+$). Under the effect of the internal electric field, the electrons at *CB* of Co_3O_4 migrated to *CB* of BMO, since the potential for e^- (-0.53 eV vs. NHE) is more negative than that of $O_2/\cdot O_2^-$ (-0.33 eV vs NHE, pH= 7). Therefore, the electrons combined with the dissolved O_2 and produced $\cdot O_2^-$ radicals ($O_2 + e^- \rightarrow .O_2^-$). At the same time, photo-induced holes (h^+) were delivered from *VB* of BMO to that of Co_3O_4. Because the potential of *VB* of Co^{3+} (2.36 eV) is higher than $\cdot OH/OH^-$ (1.99 eV vs NHE, pH = 7) [35], thus h^+ oxidized the OH^- or H_2O into $\cdot OH$ radicals at the *VB* of Co^{3+}.

On the other hand, Co^{2+} ions with smaller (0.46 eV) band gap energy acted as a shallow energy state and accelerated the electron transfer to the *CB* of BMO as well. In addition, the fermi level of Au NPs is less negative than *CB* of BMO (-0.35 eV) and higher than *VB* of Co_3O_4. Evidently, this potential difference thermodynamically promoted the electrons at *CB* of BMO and holes at *VB* of Co_3O_4 easily and faster migrated into the Au surface through Schottky barrier before their recombination. The OVs are shallow defects as well which would form a sub-band above *VB* of BMO.

Thirdly, holes with strong oxidation power and electrons having strong reduction power participated in photocatalytic reactions, they effectively degraded the organic pollutants and increased the e^-/h^+ pairs consumption ($O_2^-/.OH/h^+ + MO \rightarrow CO_2 + H_2O$).

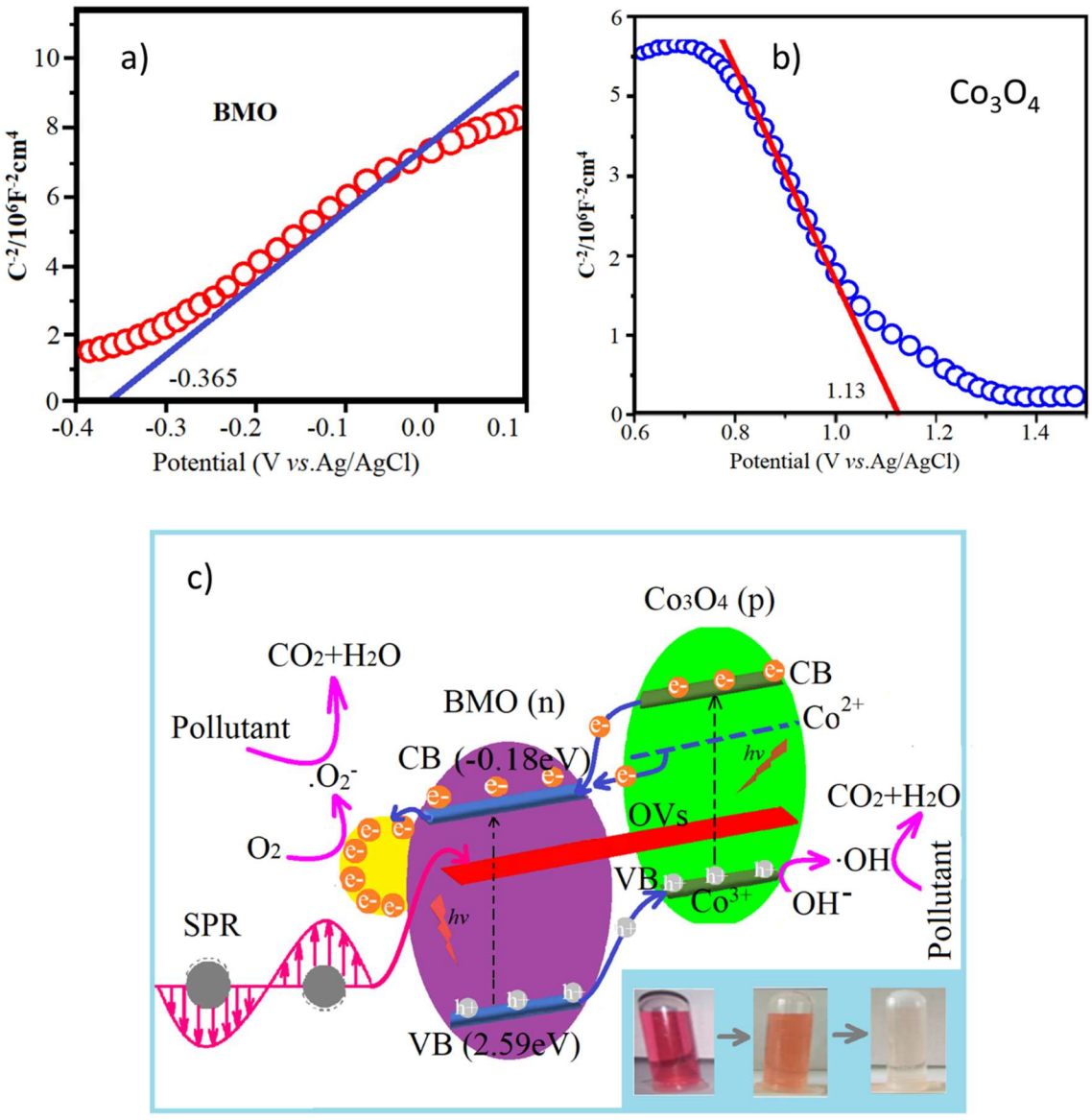

Fig.15- Mott-Schottky curves of BMO(a), Co_3O_4 (b) and mechanism of hole-electron separation and transfer process for the CBMOA under visible light irradiation (c).

3.9 Possible pathway or intermediate products

The possible degradation pathway of MO using CBMOA were proposed were analyzed by LC&MS system. Through the mass spectrograms, we noticed that the characteristic peak at m/z 306 of MO disappeared after 30 minutes' reaction, and several important intermediates were produced with m/z peaks at 121, 136, 157, and 172, respectively during the process. This indicated that the sulfanilic acid (172) was fragmented into benzenesulfonic acid (157) through losing an amino group (NH_2), while the N,N-dimethyl-p-phenylenediamine at m/z (136) was fragmented into N,N-dimethylbenzenenamine at m/z (121) after losing an amino group (NH_2) [41]. Therefore, we proposed a possible pathway of MO degradation in Fig.16. The MO was most likely degraded through breaking symmetric cleavage of the azo bond (–N=N–); producing sulfanilic acid and N,N-dimethyl-p-phenylenediamine. Finally, these intermediates products were further mineralized into CO_2 and H_2O under the presence of •OH, O_2^-radicals.

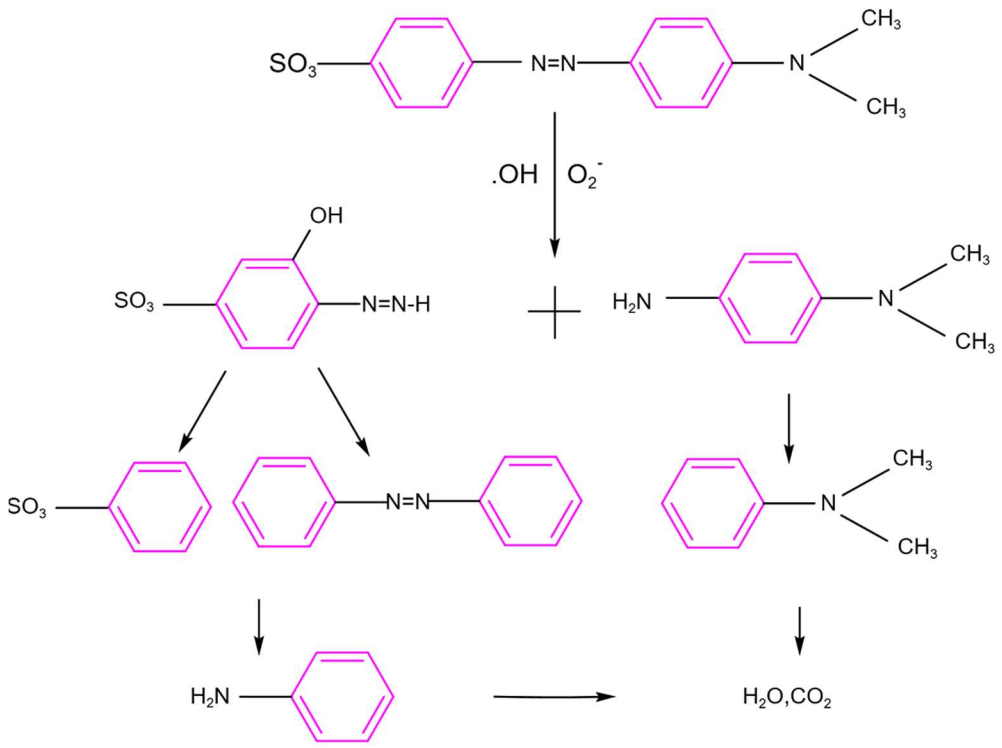

Fig.16- Possible pathway for degradation of methyl orange (MO) by CBMOA

3.10 Magnetic properties

The magnetic performance was measured to study the influence of anchoring of Au and grafting of Co_3O_4 to BMO. Figs.17a and 17b present the *M-H* hysteresis loops at 300 K and *M-T* curves of samples under 0.5 mT magnetic field. All samples exhibited ferromagnetism with typical *M-T* curves. Among them, the CBMOA displayed the strongest ferromagnetism performance. As can be seen, the saturation magnetization (M_s) of BMO was very weak due to the nonmagnetic Mo^{6+} ions. However, the magnetism at room temperature was significantly enhanced by the grafting of Co_3O_4 and particular the anchoring of Au NPs. The reason behind this improvement was due to

the contribution from magnetic ions with unfilled 3*d* bands and Au nanoparticles with 4*d* bands electrons.

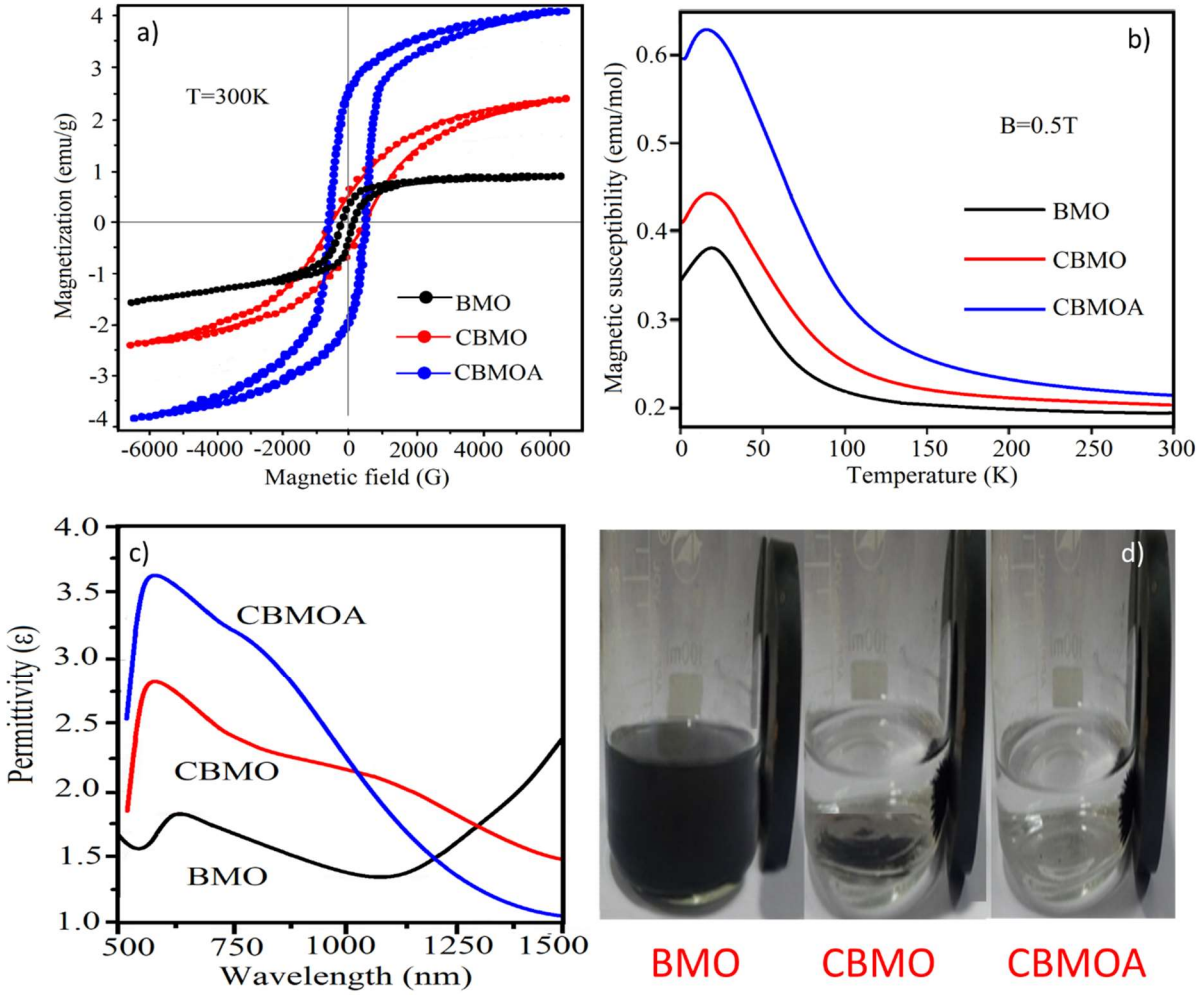

Fig.17- *M-H* loop (a), *M-T* loop (b), permittivity versus wavelength (c) and separation photographs (d) of samples

The reason behind the much higher M_s and M_r of CBMOA than CBMO was further investigated using optical dielectric permittivity measurement. The optical dielectric permittivity was evaluated using a spectroscopic ellipsometer (JA Woollam RC2). Previous study on EPR and DOS of samples have confirmed the influence of Au NPs to spin states and 3*d* orbital electrons of Co ions, respectively. In addition, from the third-order nonlinearity study, the Au NPs anchoring greatly increased the polarizability of CBMOA. As can be seen from Fig.17c, the anisotropy in optical permittivity of CBMOA is much larger than that of CMBO and BMO. This is because Co_3O_4 and Au NPs reduced the E_g which further gave rise to the lower out-of-plane permittivity and thus

enhanced the anisotropy, especially in the higher wavelength region [18]. Another important feature of Fig.17c was the permittivity continuously decreased as wavelength increasing, resulting in an increase of anisotropy in the near infrared wavelength region. The increase of permittivity and anisotropy suggested that the CBMOA sample behaved more metallic in magnetic direction, which explained well why the magnetization of CBMOA was much stronger than that of CBMO, even though two samples owned the same magnetic ions concentration (Co ions).

In addition, under applied magnetic field, CBMOA having high anisotropy and high polarizability which have paved an easier and more efficient pathway for magnetic dipoles to align themselves with magnetic field, thus leading to a larger M_s and M_r. The magnetic and permittivity study in Fig.17c revealed that, the incorporation of magnetic particle (Co_3O_4) has endued the samples with magnetic properties, and the anchoring of Au metal sharply increased the polarizability and optical anisotropy. All of these made it much easier for separation and recovery during practical synthesis and applications (Fig.17d). Table 2 reported the optical, magnetic and photocatalytic parameters of three samples, and the CBMOA exhibited 4 folds higher degradation efficiency and 2.7 folds higher photocurrent density than pure BMO.

Table 2- The specific surface area (*SSA*) (absorption coefficient (α), cutoff wavelength (λ), energy band gap (E_g), polarizability (α_{O2-}), nonlinear absorption coefficient (α_3), saturation magnetization (M_s), remanance magnetization (M_r) photocurrent (A) and photocatalytic degradation efficiency (η) of samples.

Sample	*SSA* m^2/g	α(cm^{-1}) ±0.0001	λ(*nm*) ±1	E_g(eV) ±0.1	$\alpha_3\times10^{-10}$ (m/W)	*Ms*±0.01 *(emu/g)*	*Mr*±0.01 (*emu/g*)	*A* ±1 *(mA/g)*	η ±1 (%)
BMO	30.60	0.1314	447	2.77	1.14	1.93	0.22	62	22
CBMO	42.82	0.2095	473	2.62	2.28	2.39	0.41	101	48
CBMOA	83.64	0.4662	560	2.20	5.66	4.08	3.54	176	92.2

4. Conclusion

In conclusion, Au nanoparticle doped p-n heterostructured Co_3O_4 /Bi_2MoO_6 (CBMO) catalyst was synthesized. SEM, TEM, XRD and Raman/FT-IR spectra observation of Au/Co_3O_4/Bi_2MoO_6 (CBMOA) displayed nanosheets-composed hierarchical microsphere structure with Au and Co_3O_4 crystals attached on surface. XPS spectra revealed the chemical binding energy states of constituted components, verifying the metallic Au and Co_3O_4 with expected Co^{2+}: Co^{3+} ratio. The N_2 adsorption BET test indicated that the incorporation of Au NPs and Co_3O_4 enlarged the specific surface area which was good for organic pollutants degradation. CBMOA exhibited a remarkable photocatalytic performance for Methy orange with 4-fold higher degradation efficiency and 2.7-fold larger photocurrent intensity than pure Bi_2MoO_6. Colorless phenol was subjected to photocatalytic test to further confirm the good degradation efficiency. The reason was explained through Mott-Schottky curves and various techniques. Active-species trapping experiments by EPR revealed the radicals corresponding for photo-catalysis were $.O_2^-$,.OH and OVs which exhibited a pronounced increase intensity in CBMOA, demonstrating the Co_3O_4, Au NPs and OVs contributed the good photocatalytic activity. Furthermore, energy band gap obviously decreased in CBMOA which matched DFT calculation very well. The possible influential reasons for

photocatalytic activity were thoroughly studied. The results indicated that the enhancement of photocatalytic performance was ascribed predominantly to the synergistic effect between Au SPR, hetero-structured Co_3O_4 with multivalence states and SPR induced oxygen vacancies. The SPR effect not only increased and broadened the visible light absorption capability and range, and thereby facilitated the oxygen activation, but also activated the O2p and Co3d electrons near Fermi level and improved the separation and migration of e^-/h^+ pairs. This work has provided a promising route for developing new photo-catalysts with additional functions for degradation of organic pollutants.

Acknowledgement

This study would acknowledge the financial supports from project 21A430009 based on Henan International Joint Laboratory of Nano-Photoelectric Magnetic Materials and Basic research projects of Shenzhen virtual university peak (Free exploration type 2021Szvup155).

Conflict of Interest:

There is no conflict of interests in this article.

References

[1] Francielle Stelo, Natalya Kublik, Sajjad Ullah, Heberton Wender, Recent advances in Bi_2MoO_6 based Z-scheme heterojunctions for photocatalytic degradation of pollutants, J. Alloy Compd., 829 (2020)154591

[2] Chunchun Wang, Mingjie Cai, Yanping Liu, Fang Yang, Huiqiu Zhang, Jianshe Liu, Shijie Li, Facile construction of novel organic–inorganic tetra (4-carboxyphenyl) porphyrin/Bi_2MoO_6 heterojunction for tetracycline degradation: Performance, degradation pathways, intermediate toxicity analysis and mechanism insight, J. Colloid Interface Sci., 605(2022)727

[3] Zhao Li, Renji Zheng, Shujuan Dai, In-situ mechano-chemical fabrication of p-n $Bi_2MoO_6/CuBi_2O_4$ heterojunctions with efficient visible light photocatalytic performance, J. Alloy Compd., 882(2021)160681

[4] Chaoyang Sun, Qiuhua Xu, Yu Xie, High-efficient one-pot synthesis of carbon quantum dots decorating Bi_2MoO_6 nanosheets heterostructure with enhanced visible-light photocatalytic properties, J. Alloy Compd., 723, (2017)333-344

[5] Shijie Li, Chunchun Wang, Mingjie Cai, Fang Yang, Yanping Liu, Jialin Chen, Peng Zhang, Xin Li, Xiaobo Chen, Facile fabrication of TaON/Bi_2MoO_6 core–shell S-scheme heterojunction nanofibers for boosting visible-light catalytic levofloxacin degradation and Cr(VI) reduction, Chem. Eng. J., 428(2022)131158

[6] Ruoxu Wang, Pengfei Zhu, Ming Duan, Jing Xu, Synthesis and characterization of successive Z-scheme CdS/Bi_2MoO_6/BiOBr heterojunction photocatalyst with efficient performance for antibiotic degradation, J. Alloy Compd., 870(2021)159385

[7] Shijie Li, Chunchun Wang, Yanping Liu, Mingjie Cai, Yaning Wang, Huiqiu Zhang, Yang Guo, Wei Zhao, Zhaohui Wang, Xiaobo Chen, Photocatalytic degradation of tetracycline antibiotic

by a novel $Bi_2Sn_2O_7/Bi_2MoO_6$ S-scheme heterojunction: Performance, mechanism insight and toxicity assessment, Chem. Eng. J., 429(2022)132519

[8] Shijie Li, Xiaofeng Shen, Jianshe Liu, Lisha Zhang Synthesis of Ta_3N_5/Bi_2MoO_6 core–shell fiber-shaped heterojunctions as efficient and easily recyclable photocatalysts, Environ. Sci.: Nano, 4(2017)1155

[9] Qiuping Li, Faqian Liu, XianLian Mu, Co_3O_4/CdS energy-storing nanocomposite: A promising photoanode for photoelectrochemical cathodic protection in the dark, J. Alloy Compd., 870(2021)159340

[10] Jie Guo, Chun-Hui Shen, Jie Sun, Highly efficient activation of peroxymonosulfate by Co_3O_4/ Bi_2MoO_6 p-n heterostructure composites for the degradation of norfloxacin under visible light irradiation, Sep. Purif. Technol., 259 (2021) 118109

[11] Zhipeng Li, Lizhi Qian, Jiayuan Chen, Hydrazine hydrate reduction-induced oxygen vacancy formation in Co_3O_4 porous nanosheets to optimize the electrochemical lithium storage, J. Alloy Compd., 861(2020)157994

[12] Jinhong Bi, Wei Fang, Li Li, Xiaofen Li, Ternary reduced-graphene-oxide/Bi_2MoO_6/Au nanocomposites with enhanced photocatalytic activity under visible light, J. Alloy Compd., 649 (2019) 28-34

[13] Zemin Zheng, Huiyong Li, Xudong Zhang, Hao Jiang, High-absorption solar steam device comprising Au@Bi_2MoO_6-CDs: Extraordinary desalination and electricity generation, Nano Energy, 68(2020)104298

[14] Li Guo, Qiang Zhao, Huidong Shen, Ultrafine Au nanoparticles anchored on Bi_2MoO_6 with abundant surface oxygen vacancies for efficient oxygen molecule activation, Catal. Sci. Technol., 9(2019) 3193

[15] Shijie Li, Shiwei Hu, Wei Jiang, Junlei Zhang, Kaibing Xu, Zhaohui Wang, In situ construction of WO_3 nanoparticles decorated Bi_2MoO_6 microspheres for boosting photocatalytic degradation of refractory pollutants, J. Colloid Interface Sci., 556(2019) 335-344

[16] Q. Feng, Y.Y. Li, G. Shi, photo-controllable third-order nonlinear optical (NLO) switch based on a rhodamine B salicylaldehyde hydrazone metal complex, J. Mater. Chem. C, 4 (2016) 8552

[17] V. Umapathy, A. Manikandan, Structure, morphology and opto-magnetic properties of Bi_2MoO_6 nano-photocatalyst synthesized by sol−gel method, Trans. Nonferrous Met. Soc. China, 25(2015) 3271

[18] Jie Ding, Zhiquan Yang, Chong He, Xiaowen Tong, Ying Li, Xiaojun Niu, Hongguo Zhang, UiO-66(Zr) coupled with Bi_2MoO_6 as photocatalyst for visible-light promoted dye degradation, J. Colloid Interface Sci., 497(2017)93

[19] Chengcheng Zhao, Changlu Shao, Xinghua Li, Magnetically separable $Bi_2MoO_6/ZnFe_2O_4$ heterostructure nanofibers: Controllable synthesis and enhanced visible light photocatalytic activity, J. Alloy Compd., 747(2018)916

[20] Kaixiang Xia, Hanxiang Chen, Designing visible-light-driven Z-Scheme catalyst 2D g-C_3N_4/ Bi_2MoO_6: enhanced photodegradation activity of organic pollutants, Phys. Status Solidi A, 3(2018) 1800520

[21] Bilal M. Pirzada, Pushpendra, Ravi K. Kunchala, and Boddu S. Naidu, Synthesis of $LaFeO_3$/Ag_2CO_3 Nanocomposites for photocatalytic degradation of rhodamine B and p-Chlorophenol under natural sunlight, ACS omega, 4,2 (2019)2618

[22] Wei Zhang, Boddu S. Naidu, Jian Zhen Ou, Anthony P. O'Mullane, Liquid metal/metal oxide frameworks with incorporated Ga_2O_3 for photocatalysis, ACS applied materials & interfaces, 7,3 (2015)1943

[23] Tianjin Ma, Juan Wu, Yidong Mi, Qinghua Chen, Novel Z-scheme g-C_3N_4/C@ Bi_2MoO_6 composite with enhanced visible-light photocatalytic activity for b-naphthol degradation. Sep. Purif. Technol., 183(2017)54.

[24] Zaiwang Zhao, Wendong Zhang, Bi Cocatalyst/ Bi_2MoO_6 microspheres nanohybrid with SPR-promoted visible-light photocatalysis, J. Phys. Chem. C, 120, 22(2016)11889–11898

[25] Anukorn Phuruangrat, Sunisa Putdum, Hydrothermal synthesis of Bi_2MoO_6 visible-light-Driven photocatalyst, J. Nanomater, 135735(2018)1

[26] Tiantian Feng, Hao Yin, Hao Jiang, Design and fabrication of polyaniline/ Bi_2MoO_6 nanocomposites for enhanced visible-light-driven photocatalysis, New J. Chem., 43(2019) 9606

[27] Anukorn Phuruangrat, Nuengruethai Ekthammathat, Hydrothermal synthesis, characterization, and optical properties of Ce doped Bi_2MoO_6 nanoplates, J. Nanomater, 934165(2014)1

[28] V G Hadjievl, M N Ilie, The Raman spectra of Co_3O_4, J. Phys. C: Solid State Phys., 21 (1988) 199

[29] A. Diallo, A.C. Beye, T.B. Doyle, Green synthesis of Co_3O_4 nanoparticles via aspalathus linearis: physical properties, Green Chem. Lett. Rev., 8(2015)30

[30] Zan Dai, Fan Qin, Huiping Zhao, Crystal defects engineering of aurivillius Bi_2MoO_6 by Ce doping for increased reactive species production in photocatalysis, A*CS Catal.*, 6, 5(2016)3180

[31] Ruiqi Wang, Duanyang Li, Hailong Wang, Preparation, characterization, and performance analysis of S-doped Bi_2MoO_6 nanosheets, Nanomaterials 9(2019) 1341

[32] Qiuling Chen, Pengxian Lu, Yinlei Hao, Morphology, structure and properties of Bi_2S_3 nanocrystals: role of mixed valence effects of cobalt, J Mater Sci: Mater Electron, 32(2021)24459

[33] Shi-Yuan Zhang, Ting-Ting Li, Co_3O_4 polyhedrons with enhanced electric conductivity as efficient water oxidation electrocatalysts in alkaline medium, J Mater Sci., 53(2018)4323

[34] Ganhua Qiu, Renshan Wang, One-Step synthesized Au−Bi_2WO_6 Hybrid nanostructures: synergistic effects of Au nanoparticles and oxygen vacancies for promoting selective oxidation under visible light, Ind. Eng. Chem. Res., 58(2019)17389

[35] Feng Fu, Huidong Shen, Xiang Sun, Synergistic effect of surface oxygen vacancies and interfacial charge transfer on Fe(III)/ Bi_2MoO_6 for efficient photocatalysis, Appl. Catal. B, 247(2019)150

[36] Wenli Zhao, Xu Wang Wenliang, Wang, Fabrication of oxygen vacancy-rich 3D/2D Bi1-XBr/BiOCl heterostructures towards efficient charge separation for enhanced photodegradation activity, Mater. Res. Bull., 143(2021) 111448

[37] Francis Opokua, Krishna Kuben Govender, Insights into the photocatalytic mechanism of mediator-free direct Z-scheme g-C_3N_4/ Bi_2MoO_6 (010) and g-C_3N_4/Bi_2WO_6 (010) heterostructures: A hybrid density functional theory study, Appl. Surf. Sci., 427(2018)487

[38] Roberto Núnez-Gonzalez, R. Range, DFT study of electronic structure and optical properties of Ru-doped low-temperature γ- Bi_2MoO_6 phase, Solid State Commun., 318 (2020) 113978

[39] Huidong Shen, Wenwen Xue, Efficient degradation of phenol and 4-nitrophenol by surface oxygen vacancies and plasmonic silver co-modified Bi_2MoO_6 photocatalysts, chem., 10,24 (2018) 18463

[40] Piotr Pietrzy and Zbigniew Sojka, Co^{2+}/Co^0 redox couple revealed by EPR spectroscopy triggers preferential coordination of reactants during SCR of NOx with propene over cobalt-exchanged zeolites, Chem. Commun., 2(2007)1930

[41] Masaku Kgatle, Keneiloe Sikhwivhilu, Degradation kinetics of methyl orange dye in water using trimetallic Fe/Cu/Ag nanoparticles, Catalysts, 11(2021)428